

Simultaneous 5 kHz OH-PLIF/PIV for the study of turbulent combustion at engine conditions

Carson D. Slabaugh · Andrew C. Pratt ·
Robert P. Lucht

Received: 21 May 2014 / Accepted: 30 October 2014 / Published online: 19 November 2014
© Springer-Verlag Berlin Heidelberg 2014

Abstract Simultaneous measurements of velocity and scalar fields were performed in turbulent nonpremixed flames at gas turbine engine-operating conditions using 5 kHz particle image velocimetry (PIV) and OH planar laser-induced fluorescence (OH-PLIF). The experimental systems and the challenges associated with acquiring useful data at high pressures and high thermal powers are discussed. In this work, a wide range of operating conditions were studied, with a maximum pressure and thermal power of 1.8 MPa and 950 kW, respectively. In the PIV measurements, the high thermal power conditions were shown to cause significant defocusing of the particle images. This was the result of variations in the optical refractive index of the gas which were caused by strong temperature gradients within the inner structure of the flame. High flame luminosity also led to decreased SNR with increasing flame power. The OH-PLIF measurements did not show indication of strong laser sheet absorption at any condition tested. However, a decrease in the peak SNR was observed with increasing chamber pressure. An analysis of the true measurement resolution with respect to the scales of the flow is also given. Based on the resolved scales, the present dataset was used to study the time-averaged flow structure and its effect on flame behavior. Heat release conditioned flow statistics were studied to elucidate the flow–flame interactions in high-power flames.

1 Introduction

As massively parallel numerical simulations become increasingly common, Large Eddy Simulations (LES) have begun to evolve from the research domain into the industrial sector. These computations have the *potential* to provide fully unsteady, four-dimensional results on the turbulent reacting flows found in modern combustion systems. However, the complexities of such simulations are immense, with fully coupled, multi-physical interactions occurring over a very broad range of spatial and temporal scales. To validate these difficult computations, there is great need for complementary experimental measurements with high dimensionality and high resolution (in both space and time) acquired at the extreme conditions of engine operation.

The key challenge to making measurements in any turbulent reacting flow is to sufficiently resolve the broad spectrum of spatial and temporal scales over which the rate-controlling processes occur. A nonergodic dynamical system of coupled physical and chemical interactions, these processes govern the structure of the turbulent flow, the progress of chemical reaction, and the stabilization of the flame. The spectrum of scales which characterize a turbulent flow is defined by the geometry of that flow and the dissipation of turbulence energy through viscosity. The range of scales associated with chemical phenomena controlling combustion processes are governed by the local gradients in mass fraction, temperature, and density. Depending on the local manifestations, coupled interactions between the turbulence field and chemical reactions can lead to largely different results. For example, the presence of turbulence can amplify local heat release at a reaction front by wrinkling the flame and increasing the surface area. On the other hand, if the turbulence is too strong, it

C. D. Slabaugh (✉) · A. C. Pratt · R. P. Lucht
School of Mechanical Engineering, Purdue University, 585
Purdue Mall, West Lafayette, Indiana 47906, USA
e-mail: cslabau@purdue.edu

can lead to local extinction through quenching. The flame will also have an effect on the turbulence field. Flame-generated turbulence is the result of flow acceleration across the reaction front, caused by the rapid change in gas density, which leads to amplification of the velocity gradients. As a competing effect, the increased kinematic viscosity in the burnt gases can act to dampen these fluctuations through increased molecular dissipation. Randomness and nonlinearity in the coupling of these turbulence–chemistry interactions can even result in all four cases being concurrently present in the same turbulent reacting flow [1–6].

This description serves to illustrate that experimental measurements in turbulent flames are concomitant with very difficult requirements for the resolution and dynamic range of the applied diagnostic techniques. In practical flames, these challenges are exacerbated. Among other factors, these flames are characterized by a high thermal power density, which is achieved, in part, by a high turbulence Reynolds number, Re_t (where $Re_t = Re(l_t) = u'l_t/\nu$, where l_t is the integral length scale). As the turbulence Reynolds number is increased, the spectrum of coherent structures within the flow becomes broader, scaling with $(Re_t)^{\frac{3}{4}}$. Enhancing the transport of mass, momentum, and heat within the flame, this effect further broadens the spectrum of scales over which the rate-controlling processes within the flame occur.

Laser-based measurement techniques provide a non-intrusive means of collecting quantitative data in a turbulent reacting flow field. For many years, researchers relied on stochastic or (at best) phase-locked measurements to study the highly unsteady flow field, thermo-chemical, and thermo-acoustic physics present in turbulent reacting flows. The temporal resolution of these systems was limited by the repetition rate of the flashlamp-pumped Nd:YAG lasers available at the time, which can provide high single-pulse energy, but little to no tunability of the interrogation frequency. Early efforts to improve the temporal resolution of laser-based measurements were accomplished utilizing clusters of these low-repetition-rate, flashlamp-pumped systems. With this architecture, the timing of the pulses from each individual laser is controlled to achieve burst of pulses with closely spaced time separation, albeit for a limited number of pulses (limited by the number of lasers in the cluster). With this approach, Kaminiski et al. demonstrated high-speed OH-PLIF imaging measurements acquired with a time separation of 125 μs for a series of eight images [7]. One key advantage of the *pulse-burst* approach is that improved temporal resolution can be achieved without a loss in laser pulse energy. The obvious drawback to the clustered architecture is that these systems quickly become cost-prohibitive when attempting to increase the number of laser pulses per burst. A second approach to burst-mode laser operation is to utilize a

low-power, high-repetition-rate laser source as the master oscillator, then amplify a burst-train of low-energy pulses using a series of flashlamp-pumped amplification stages [8, 9]. Recent demonstrations of a system based on this platform have shown that by utilizing a fiber oscillator and diode-pumped Nd:YAG amplifiers, a significant extension of the pulse train length can be achieved, up to 200 sequential measurements at a 20-kHz repetition rate with 150 mJ/pulse [10]. With pulse energies on the order of conventional 10 Hz systems and kHz repetition rates, these systems show great promise for planar (or even volumetric) measurements, with high temporal resolution. In their current state, however, the drawback to these systems is that they are still in a custom, research-only level of refinement. Consequently, the cost is building/owning a pulse-burst system remains quite high.

In recent years, the rapid development and commercial availability of high-repetition-rate, diode-pumped solid-state (DPSS) lasers with short pulse durations have made temporally resolved planar measurements of velocities and scalars in turbulent flows a more accessible option [11, 12]. Operating on a continuous duty cycle, the average power output from the DPSS laser systems can be quite high but the single-shot pulse energy is low (on the order of 10 mJ). Nonetheless, the reduced complexity and cost of this platform have made them quite popular, with many research groups now making measurements with multiple DPSS systems. Simultaneous integration of these systems has supported concurrent scalar and velocity field measurements at kHz interrogation frequencies in laboratory-scale flames. These efforts have yielded a greater understanding of dynamic turbulent flame behavior through tracking the temporal evolution of transient phenomena such as local extinction, auto-ignition, and turbulence–chemistry interactions [13–20].

With the advances in the quantity and depth of information that can be acquired with high-speed measurements, there has been significant interest in the extension of these capabilities from canonical, laboratory-scale flames to large-scale facilities. As eluded to previously, improved temporal resolution of combustion processes is especially desirable in flames of high thermal power density where local flow–flame interactions occur over a much larger range of spatial and temporal scales. Under such operation, unsteady local flow conditions can have strong effects on flame behavior, particularly in the case of nonpremixed combustion devices where the turbulent combustion regime is very difficult to define. Besides temporal resolution considerations, high-repetition-rate measurement techniques have a more practical advantage in that they facilitate the rapid accumulation of statistically significant datasets. While seemingly obvious, this fact should not be overlooked as a key advantage when acquiring measurements

in large-scale test rigs where operational costs can exceed tens of thousands of dollars per day. In such cases, acquiring data at rates over 10^3 times faster can be a determining factor in the success of a test campaign.

While the motivation for applying these new tools is clear, there are significant challenges that must be faced as well. Though the average power output from DPSS laser is high, the single-shot pulse energy is approximately two orders of magnitude lower than that of comparable 10 Hz systems. As a result of this low pulse energy, the species which can be probed with acceptable SNR are limited [21]. Characteristically poor beam intensity profiles with strong shot-to-shot variations present additional challenges to the extraction of quantitative data when using these systems. Nonetheless, these measurement tools have the potential to provide data highly sought after by those developing computational combustion codes for use in these regimes of operation as well as providing insight to designers of practical combustion systems. In the work of Boxx et al. [22], simultaneous PIV/OH-PLIF and simultaneous PIV/OH* chemiluminescence (CL) measurements were acquired at a sustained 3-kHz repetition rate in a 120-kW flame operating at 5 bar. This work established the feasibility of making high-speed OH-PLIF measurements at these elevated conditions using the robust DPSS laser platform. The authors observed strong laser sheet absorption effects, evident through signal attenuation in the direction of the excitation beam propagation, which severely affected the SNR and the utility of the OH-PLIF data. However, it was shown that information about the large-scale dynamic behavior of the flow and flame could be extracted from the simultaneous complementary high-speed diagnostics.

In this work, the application of time-resolved diagnostics is extended to even more challenging environments

representative of those found in aeropropulsion gas turbine engines. Using more powerful DPSS lasers, the feasibility of acquiring simultaneous scalar and velocity field (OH-PLIF and PIV) measurements at 5 kHz interrogation frequency in a high thermal power density, liquid-fueled flame is demonstrated. The data quality is characterized, and an analysis of the true measurement resolution with respect to the scales of the flow is also given. A baseline analysis of the resolved scales further elucidates the flame characteristics that can be extracted from these measurements.

2 Experiment configuration

2.1 Burner and test rig

A detailed description of the experimental facility, used in this work, has been given previously [23]; hence, only a brief description of the burner and flames is provided here. The combustor is a piloted, partially premixed, swirl burner designed for operation at a high thermal power density burning liquid fuels. Dry, high-pressure, preheated air is supplied to the pilot and main air swirlers from a common manifold while fuel is delivered to the pilot and main nozzles by two independently controlled and metered circuits. The pilot channel includes two coaxial swirlers separated by a thin tube where fuel is introduced through a central fuel nozzle. The pilot fuel spray is then partially vaporized and mixed with the swirling pilot air in the pilot channel before entering the main combustion zone. The main fuel is injected radially, where it is also partially premixed and partially prevaporized with swirling main air flow before entering the main combustion zone. At the dump plane, the pilot and main channels are separated by a bluff-body ring,

Fig. 1 Schematic of the test rig and burner with diagnostic fields of view indicated

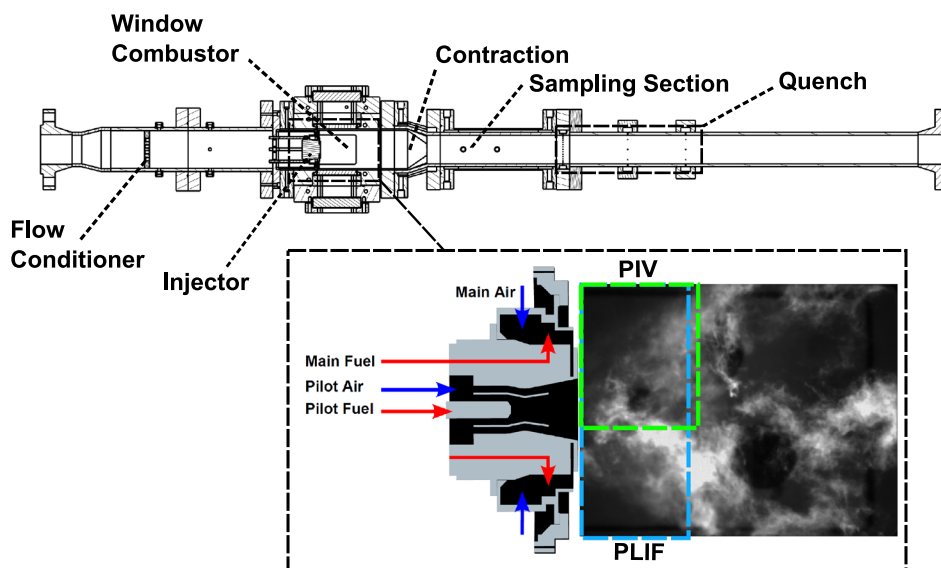


Table 1 Operating conditions studied

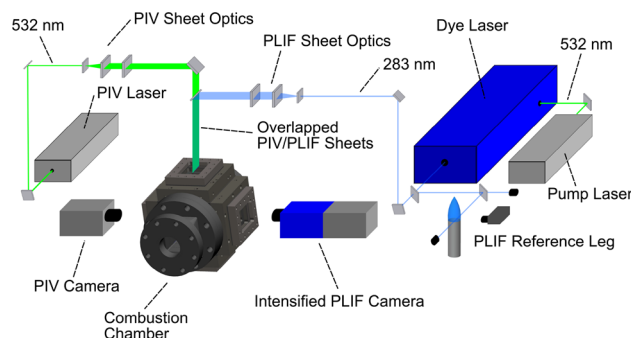
| Flame condition | Pressure (MPa) | Main air temperature (K) | Thermal power (kW) | ϕ_{global} | ϕ_{pilot} | ϕ_{main} |
|-----------------|----------------|--------------------------|--------------------|------------------------|-----------------------|----------------------|
| A | 0.6 | 700 | 350 | 0.55 | 0.75 | 0.5 |
| B | 1.0 | 700 | 550 | 0.55 | 0.75 | 0.5 |
| C | 1.4 | 700 | 700 | 0.55 | 0.75 | 0.5 |
| D | 1.8 | 700 | 950 | 0.55 | 0.75 | 0.5 |
| A-NR | 0.6 | 700 | – | – | – | – |
| B-NR | 1.0 | 700 | – | – | – | – |
| C-NR | 1.4 | 700 | – | – | – | – |
| D-NR | 1.8 | 700 | – | – | – | – |

which creates a gap of nearly ten millimeters between the two concentric nozzle exits.

As shown in Fig. 1, the burner is installed into an optically accessible, high-pressure combustion rig. All hardware throughout the *hot* sections is water-cooled, minimizing the need for dilution flows that can complicate measurements of the flame physics. The combustion chamber has a 105-mm square cross section and a length of 230 mm. Fused quartz windows provide optical access from the burner face to 100 mm downstream over approximately 80 mm of the chamber width. The exhaust is directed through a contraction (2:1) to close the central recirculation zones, which result from the swirl-induced vortex breakdown [24]. Exhaust gas sampling provides closure on the combustion process through comparison of major species concentrations measured with equilibrium calculations. After sampling, the hot gas is quenched through a three-stage water deluge.

A National InstrumentsTM-based data acquisition system is used for completely remote control of the experiment and to monitor hardware health. Data from this system are recorded at 100 Hz to document the flame conditions while optical data are collected. Kulite[®] piezoresistive pressure transducers are installed in the upstream air plenum and within the combustion chamber itself. Data from these sensors were sampled simultaneously at a 100-kHz interrogation frequency with a DSPCon[®] high-frequency DAQ. Pressure fluctuation amplitude and frequency content were monitored in real time to allow test operators to rapidly detect and avoid unstable operating conditions that could damage experiment hardware.

As the experiment is designed for steady-state operation, the flame was run continuously as optical measurements were acquired. The only limiting factor on run duration was fouling of the windows from PIV seed particles. While particle seeding time was minimized to short, ten-second bursts around the actual data acquisition, the total seeding time was limited to approximately 100 seconds at the targeted seeding densities.

**Fig. 2** Schematic of simultaneous diagnostics configuration

2.2 Flames

To study the applicability of high-repetition-rate diagnostics to turbulent flames of practical interest, four conditions were chosen. Summarized in Table 1, flames A–D vary the combustor pressure and total mass flow rates (consequently, also the thermal power) while all other flame conditions were held fixed, including the preheated inlet air temperature, the global equivalence ratio, and the pilot-to-main fuel split. Flame A was considered as a starting point for this developmental work as it most closely represented the conditions previously demonstrated in the work of Boxx et al. [22]. The severity of the conditions was then increased to conditions representative of lean cruise operation of an aerospace propulsion engine. Nonreacting PIV data were also acquired at each inlet condition. The conditions were defined by matching the temperature, pressure, and total air mass flow rate of the corresponding reacting flow conditions and are given an *NR* designation in Table 1. A Jet-A surrogate fuel was used in all of the experiments (PetroSA PS-150). It was chosen for its extremely low aromatic content <60 ppm in comparison with standard Jet-A (18–25 % by volume). The fluorescence signal of aromatic molecules is very strong compared to that of the targeted radical species making it difficult to distinguish fluorescence from the fuel and OH with the current system.

3 Diagnostic systems

As indicated in Fig. 2, the simultaneous diagnostics system is a combination of a PIV system and an OH-PLIF system. The individual systems and their simultaneous integration are described in this section.

3.1 Particle image velocimetry

A dual-cavity, diode-pumped solid-state (DPSS) Nd:YAG laser (Edgewave IS811-DE) provided 532 nm light at 4 mJ/pulse with a repetition rate of 5 kHz for the PIV measurements. The beam was expanded to approximately 30 mm in height using two cylindrical lenses ($f_{PIV,1} = -25$ mm, $f_{PIV,2} = 300$ mm) in a cylindrical telescope arrangement. A third cylindrical lens ($f_{PIV,3} = 750$ mm) was used to focus the collimated sheet just outside of the combustor to minimize particle dropout that could occur near the beam waist. The sheet width was measured by traversing a narrow slit through the sheet waist and measuring the transmitted power with a photodiode. The measured energy profile yielded a sheet thickness of approximately $630 \mu\text{m}$ (FWHM). The interpulse separation time was optimized to achieve mean particle field displacements of approximately half of the final interrogation window size. To cover the maximum dynamic range in the instantaneous velocity field measurements, an inter-frame time separation of $8 \mu\text{s}$ was chosen.

A fluidized bed was used to seed TiO_2 particles (250 nm nominal mean diameter) into the main air flow. The Stokes number of these particles was computed to be approximately 0.008, where $\text{St} = \tau_p/\tau_f$, $\tau_p \approx \rho_p d_p^2/18 \mu_g$, and $\tau_f \approx l_0/u'_{rms,max}$. The particles were introduced approximately four hydraulic diameters upstream of the burner using a counterflow injector that spanned the width of the inlet section. The average seed density within the reactant inflow was approximately 0.1 particles/pixel. The Mie scattering signal from the particle field was collected through a 105 mm focal length, $f/2.8$ objective (Nikkor AF-S Micro) and recorded with a high-speed CMOS camera (Photron SA-4). The camera had sufficient onboard memory to acquire 3,500 double-frame image pairs per run. The depth of field for the final configuration was calculated to be $750 \mu\text{m}$, which was appropriate for the measured sheet thickness to avoid imaging of illuminated particles outside of the focal plane. A custom ultra-steep band-pass filter (3 nm FWHM centered on 532 nm) was used to maximize the SNR in the highly luminous flame environments while a second high transmission ($T > 98\%$) band-pass filter was used to block the remaining range of the CMOS sensor sensitivity. The maximum array size for the PIV CMOS camera was 800×400 pixels, operating at a 5-kHz frame rate. For the field of view indicated in Fig. 1, this resulted

in an image resolution of $59.0 \mu\text{m}/\text{pixel}$ in the raw scattering images.

With this configuration, 35,000 velocity fields were acquired before the image quality was degraded due to window fouling (roughly 10 data acquisitions and 100 s of seeding time). Rapid accumulation of flow statistics with minimal concern of premature window fouling supported operation with significantly higher (volumetric) seed densities than previously attempted using low-repetition-rate systems. Consequently, the high interrogation frequencies have also been shown to support some improvement in spatial resolution as well.

3.2 Planar laser-induced fluorescence

The OH-PLIF laser system consisted of a high-repetition-rate, Q-switched, DPSS Nd:YAG pump laser (Edgewave INNOSLAB IS200-2-L) and a dye laser designed for efficient operation at low pulse energies and high average power (Sirah Credo). The frequency-doubled output from the pump laser provided 13.1 mJ/pulse at 5 kHz (66 W average power) with a 9.2 ns pulse duration. Using Rhodamine 590 Perchlorate dye (dissolved in ethanol), the 566.4-nm fundamental wavelength was frequency-doubled to 283.2 nm to excite the $Q_1(8)$ line of the $A^2\Sigma^+(v' = 1) \leftarrow X^2\Pi(v'' = 0)$ transition. The average laser pulse energy at 283.2 nm was 1.2 mJ/pulse for 5 kHz operation (6 W average power). A reference leg was integrated to continuously monitor the dye laser power output and tune the wavelength as needed. The first surface reflection from an uncoated fused silica window directed a small amount of the total beam energy through a Bunsen flame. The resulting LIF signal generated was collected with a photomultiplier tube and the average signal monitored with an SRS BOXCAR integrator and an oscilloscope.

The PLIF excitation sheet was formed using two cylindrical lenses ($f_{PLIF,1} = -25$ mm, $f_{PLIF,2} = 300$ mm) in a cylindrical telescope arrangement, resulting in a collimated sheet height of approximately 30 mm. A third cylindrical lens ($f_{PLIF,3} = 600$ mm) was used to focus the sheet to the beam waist at the combustor centerline. The sheet thickness was measured using the same method described in the PIV section. On the combustor centerline, the sheet thickness was measured to be approximately $500 \mu\text{m}$ (FWHM). The calculated Rayleigh range for sheet waist was approximately 35 mm; therefore, it was assumed that there was minimal variation in the laser fluence across the span of the combustor. The peak laser fluence was $9 \times 10^7 \text{ W}/\text{mm}^2$.

The OH-PLIF signal was collected using a 100-mm focal length, $f/2.8$ objective lens (Cercor Sodem Type-2178). A multi-channel plate intensifier (LaVision HS-IRO) was used to amplify the signal, which was imaged by a high-speed CMOS camera (Phantom v411). The intensifier gate width

was run at the minimum value possible (100 ns) to minimize background noise from flame luminosity. An optical band-pass filter (Semrock 320/40) was used to transmit the fluorescence from the $A^2\Sigma^+(v'=1) \rightarrow X^2\Pi(v''=1)$ and $A^2\Sigma^+(v'=0) \rightarrow X^2\Pi(v''=0)$ bands occurring over the 305–320 nm range of wavelengths. The effective filter width was sufficient to block the entire wavelength range of the intensifier photocathode sensitivity, removing elastic scattering of the laser beam from the seed particles and further reducing background flame luminosity. The filter had a transmission efficiency of >98 % over the selected bandwidth and an ultra-steep transmission cutoff (<1 nm). The maximum array size for the OH-PLIF CMOS camera, operating at a 5-kHz frame rate, was 800×800 pixels. For the field of view indicated in Fig. 1, this resulted in an image resolution of $82.5 \mu\text{m}/\text{pixel}$ in the raw data images.

3.3 Alignment and synchronization

The laser sheets from the OH-PLIF system and the double-pulsed PIV system were overlapped using a dichroic beamsplitter, with high transmissivity at 532 nm and high reflectivity at 283 nm. Alignment and overlap of the laser sheets was confirmed in the near- and far field as well as spatial orientation with respect to the combustion chamber. Spatial calibration data were collected by imaging a dual-sided, dual-plane dot target (LaVision Type 05). The same target was used for the PIV and PLIF imaging systems; thus, spatial alignment of the two measurement fields was achieved by mapping to the same coordinate system. A custom fixture was fabricated to traverse the dot target within the combustor using a series of manual linear and rotational stages. Temporal synchronization of the lasers and imaging systems was accomplished with a master timing box (Quantum Composers Model 9528). The 283-nm OH-PLIF laser pulse was delayed from the first 532 nm PIV pulse by $\Delta t/2$ ($4 \mu\text{s}$), which is the assumed time of the measured PIV vector field. Laser pulse timing was continuously monitored throughout the test using an array of photodiodes and an oscilloscope.

4 Measurement demonstrations

4.1 5 kHz particle image velocity

Particle image velocimetry (PIV) is a very robust technique that can be utilized to measure the velocity field in complex flows. The working principle of the technique is to introduce seed particles into the flow, measure their displacement over a known period of time, and then directly compute the velocity. One point of obvious, but critical, importance is that the chosen seed particles must be able

to accurately track the velocity field. In chemically reacting flows, achieving these criteria can be quite challenging as the flow will have regions of local heat release which lead to a rapid change in the flow temperature, resulting in a sharp gradient in gas density. As a result of this rarefaction, the seed particle density in the flow is decreased, which can lead to a reduced signal-to-noise ratio (SNR) in the displacement calculations. A more subtle problem comes as a consequence of the strong local acceleration of the flow. To accurately measure the flow velocity in these regions, the time scale of the particle response must be small in comparison with the time scales of the local flow velocity fluctuations (see Sect. 3.1) [25–30].

In flames operating at a high thermal power density, the turbulence Reynolds number (Re_t) is very high, amplifying the challenges previously identified as a result of the broadened spectrum of spatial and temporal scales to be resolved. Enclosed test sections also present a more practical challenge for this technique due to the fact that reflections and scattered light from internal surfaces are at the same wavelength as the signal, eliminating the possibility of spectrally filtering these noise sources from the particle field. High flame luminosity can also lead to an increased level of systematic noise, but this can be mostly eliminated by optical filtering.

4.1.1 Image preprocessing and vector generation

Figure 3a represents a typical raw, single-frame image of the scattering field from the seeded nonreacting flow. The uniformity of the seed density and minimal variation in particle size indicate acceptable seeder performance, although the detector resolution does not support a more detailed characterization of the (sub-pixel) particle size distribution.

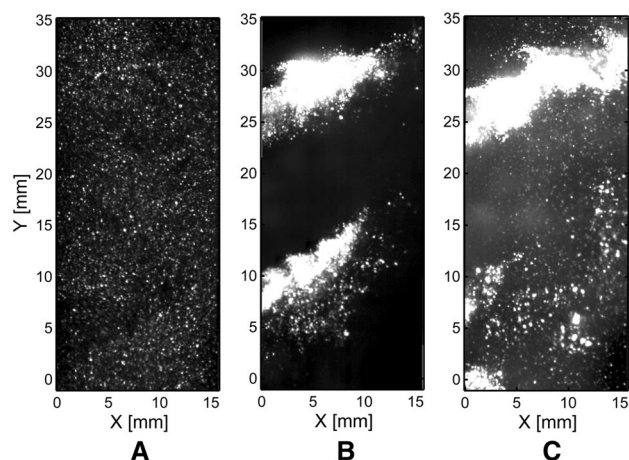


Fig. 3 Single-shot scattering images for **a** seeded nonreacting (condition B-NR), **b** unseeded reacting (condition B), and **c** seeded reacting (condition B) flows

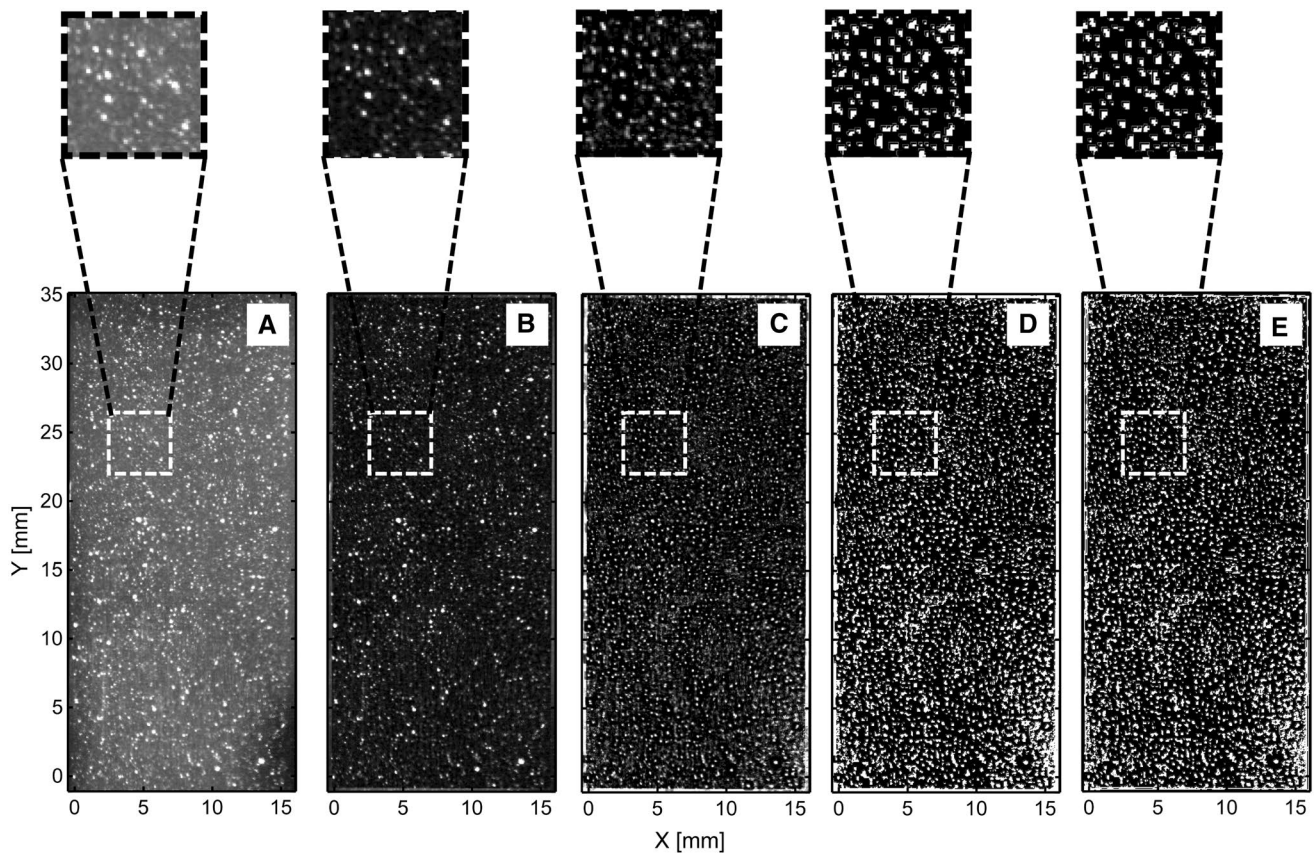


Fig. 4 PIV image-preprocessing validation on nonreacting flow (condition B-NR): **a** raw image, **b** background subtracted, **c** normalized, **d** binarized, **e** filtered

Figure 3b is a single-shot image of laser light scattering from the reacting flow field with no particle seeding where the presence of liquid fuel droplets is clearly seen in the pilot and main reactant supplies. Figure 3c shows a typical single-shot scattering image of the seeded reacting flow where the droplet presence remains clearly pronounced.

Without detailed foreknowledge of the liquid droplet size characteristics, it cannot be assumed that the Stokes number of the individual droplets will be appropriate to accurately track the gas velocity field. An image-preprocessing algorithm was developed to remove regions of the seeded scattering field where the *particle* size was too large. The basic operations of the procedure are demonstrated on a single-shot image taken from condition B-NR in Fig. 4. Local minimum subtraction, using a sliding square kernel, removes the scattering noise from reflections within the combustion chamber and background flame luminosity (in reacting cases). The kernel size used for condition B-NR was 9×9 pixels, but this is determined on a case-by-case basis by simple visual evaluation of the particle images. Normalization by the ratio of the sliding local maximum (same kernel size) to the global maximum improves the contrast of smaller and weakly illuminated

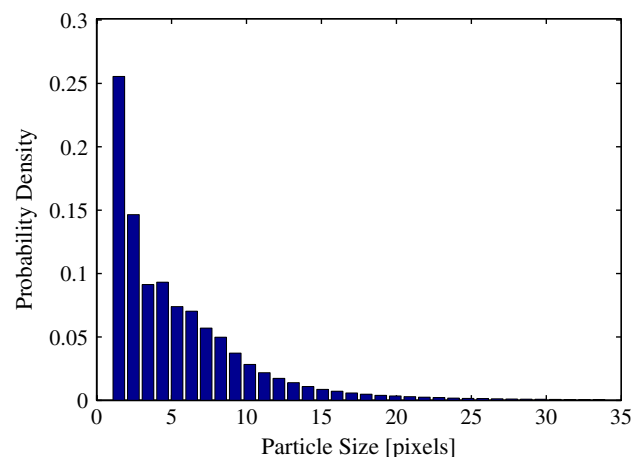


Fig. 5 Particle size PDF from seeded nonreacting flow after local background subtraction

particles (Fig. 4c) before binarization at a defined intensity threshold (Fig. 4d). The binary images are filtered using a sliding kernel which locally masks the regions where the particle size is greater than a set threshold. Note that the

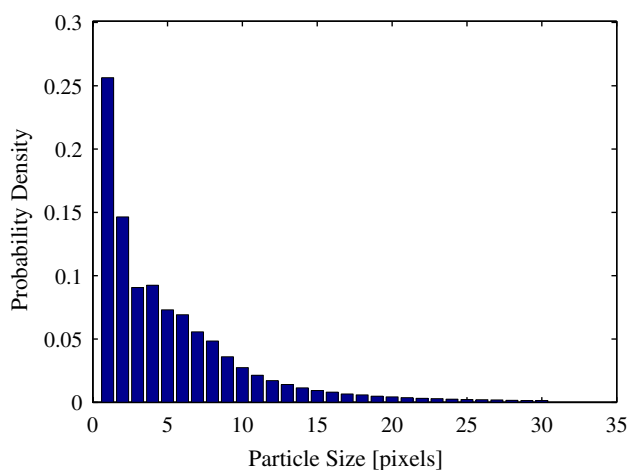


Fig. 6 Particle size PDF from seeded nonreacting flow after full preprocessing procedure

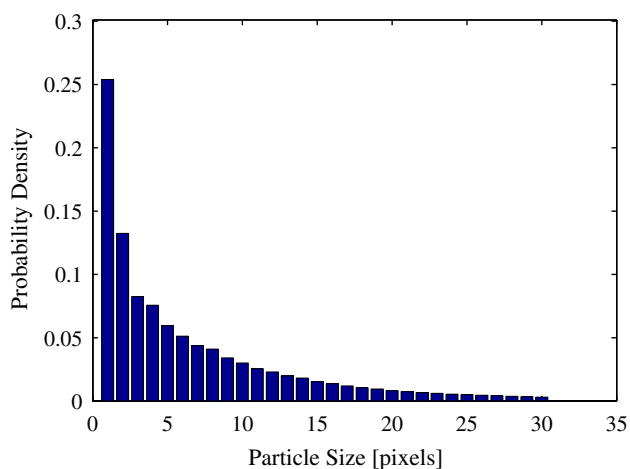


Fig. 7 Particle size PDF from seeded reacting flow after full preprocessing procedure

filtered binary image (Fig. 4e) remains unchanged from the unfiltered binary image.

To quantify the effects of these operations, it is necessary to perform a statistical analysis on the particle images. To begin, the particle size distribution was computed for the sequence of images at each preprocessing step. The computation was performed by binarization of the image at a defined threshold (at steps b and c), then summing the locally connected logical 1 pixels. Variation of the defined intensity threshold (within reasonable limits) was found to have no significant effect on the final results because the particle intensity threshold defined to determine the particle size was held equal to the threshold used in the binarization preprocessing operation (D).

Figure 5 presents the particle size distribution computed from a 7,000-frame dataset acquired at condition B-NR,

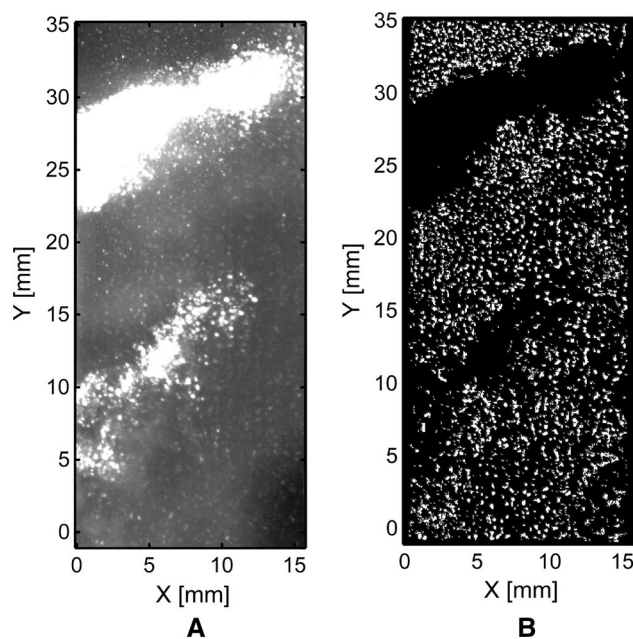


Fig. 8 PIV image preprocessing performed on reacting flow with high droplet density: raw data (a) and fully preprocessed (b)

after local background subtraction. Summation of the probability density reveals that 68 % of the imaged particles were <5 pixels in total size, 89 % were smaller than 10 pixels, >99.99 % were <30 pixels in total size. After the complete preprocessing operation (shown in Fig. 4), there is no significant change in the shape of the distribution (see Fig. 6) for a fixed binarization threshold.

Utilizing the nonreacting particle size data, the size threshold for the droplet filter was set to 30 pixels. The filtered particle size distribution in the seeded reacting flow (condition B) is given in Fig. 7. There is a slight shift in the distribution, with 60 % of the particles being smaller than 5 pixels and 78 % <10 pixels in total size. This increase in the imaged particle size is attributed to refractive index variation in the reacting flow (discussed in further detail later in this work) and the lingering presence of small droplets with an imaged size below the filter threshold. Figure 8 illustrates the final effect of the preprocessing procedure on an image with high droplet density. It is clear that the regions of high liquid concentration have been effectively masked; no velocity vectors will be generated in this region.

The filtered binary images are used as a mask on either the background subtracted or normalized images, based on the performance of the crosscorrelation algorithm. Figure 9 provides a comparison of two single-shot velocity fields (condition B-NR) generated from the particle image pairs preprocessed using only local background subtraction (Fig. 4a, b) and the full *large particle* filtering procedure

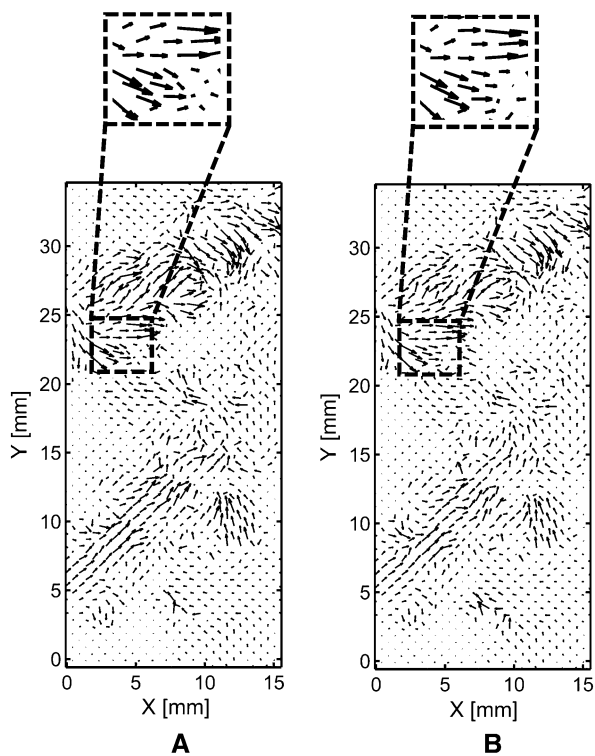


Fig. 9 Nonreacting vector field validation between vector fields generated with images preprocessed using only local background subtraction (a) and the full preprocessing procedure (b)

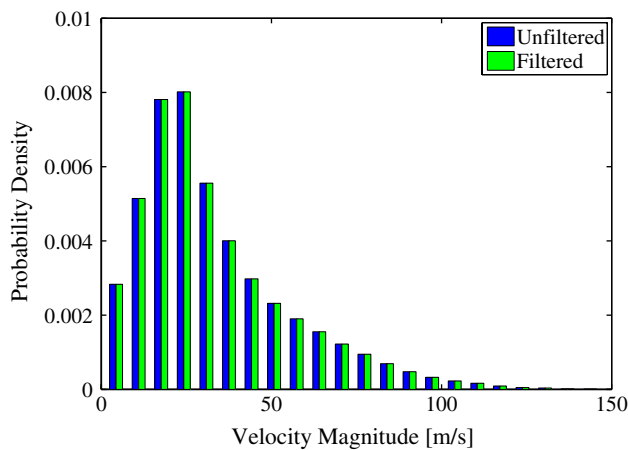


Fig. 10 Comparison of velocity magnitude PDFs in seeded, non-reacting flow for vector field processed with background subtracted (unfiltered) and fully preprocessed (filtered) images

(Fig. 4a–e). The instantaneous velocity fields are nearly indistinguishable, as expected in a nonreacting case where the filtering procedure should have little to no effect on the original data images (as shown in Fig. 4).

To quantify this result, Fig. 10 provides a comparison of the velocity magnitudes computed for the nonreacting flow

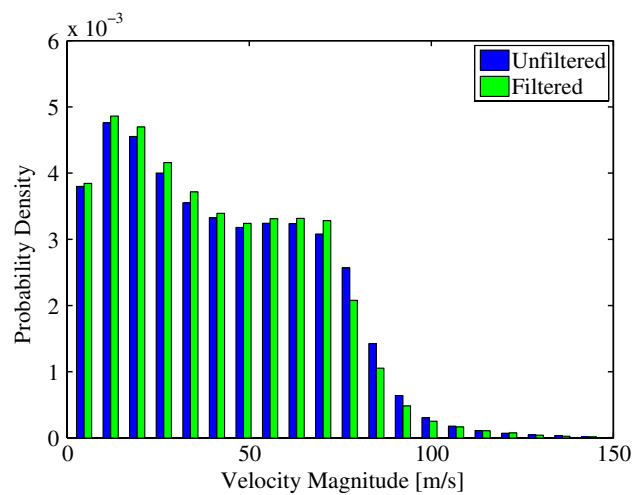


Fig. 11 Comparison of velocity magnitude PDFs in reacting flow for vector fields processed with background subtracted (unfiltered) and fully preprocessed (filtered) images

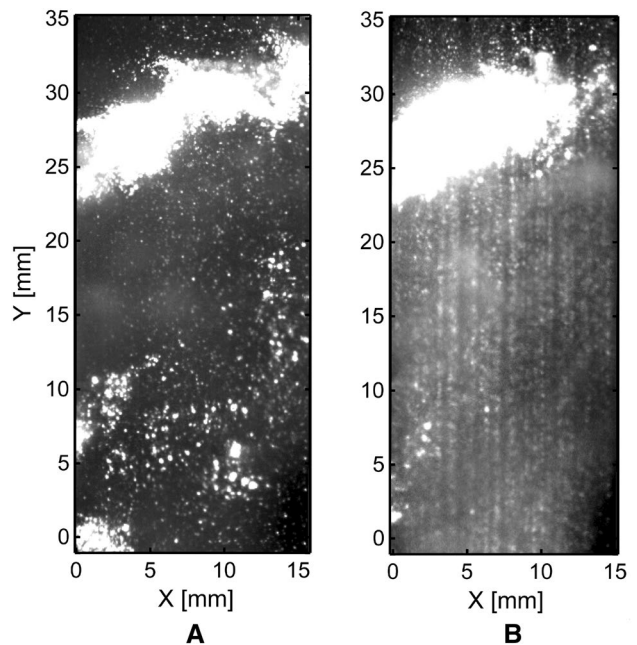


Fig. 12 Raw, single-shot, Mie scattering images from flames B (a) and D (b)

dataset (condition B-NR) with and without the 30-pixel particle size filter. There is no quantifiable change in the distribution. Figure 11 provides a similar comparison under reacting flow conditions (condition B) where the droplet presence is considerable. Note that there is a slight shift in the distribution from the high velocities (>80 m/s) to the lower velocities as a result of the droplet filtering operations. This is a result of the fact that the droplet presence in the flow is primarily limited to the reactant inflow, where

the flow velocity is high. Thus, the process induces bias into the velocity magnitude distribution by conditioning the sample with a filter that implicitly operates only on the high-velocity regions of the flow. However, the unfiltered measurements are likely to contain equal or greater errors (that are more difficult to quantify) than those induced by the filtering operations.

Figure 12 is a comparison of single-shot, preprocessed scattering images taken at flame conditions B and D. Increased luminosity from the high-power flame leads to much greater background light intensity and a reduction in the raw image SNR. It is also observed that at high thermal power density, flame D, there is significant image blur which occurs within the reaction zone of the flame, while the image remains sharp outside of the main reaction zone ($Y = 32\text{--}35$ mm). Strong spatial gradients in the gas temperature within the nonpremixed turbulent flame lead to local variation in the optical refractive index. The resultant ray steering of the scattered light signal, as it propagates through the optically inhomogeneous medium to the detector, causes the observed defocusing of the recorded image in the regions of high heat release.

The preprocessed particle images were crosscorrelated using the multi-pass adaptive window-offset algorithm in the LaVision commercial PIV software (DaVis 8.1.6). For flames A–C, a final interrogation window size of 16×16 pixels was applied, with 50 % window overlap. This resulted in a spatial vector resolution of 0.940 mm and a corresponding vector spacing of 0.470 mm. A local median filter, based on a 3×3 square kernel, was used to replace spurious vectors with an alternate correlation peak based on the velocity RMS computed within the kernel. If a replacement was not found at a secondary (or tertiary) peak, the spurious vector was replaced with an interpolated vector. Typical single-shot, reacting flow vector fields were generated with >75 % first-choice correlation peaks, approximately 15 % secondary- or tertiary-choice peaks, and < 10 % spurious vectors filtered or filled. For comparison, the nonreacting vector fields, presented in this work, were typically generated with primary contributions of 95 % (or higher) and < 2 % filtered spurious vectors. Datasets were of sufficient quality and length to achieve mean standard error convergence of < 2 %.

The accuracy of PIV displacement evaluation algorithms is a function of the uncertainty in the location of the particle image centroid and the correlation peak centroid. Thus, it was expected that the increased noise from flame luminosity and particle-defocusing effects would lead to a reduction in quality of the velocity measurements. Utilizing conditions B-NR and B as control cases, a series of systematic characterizations were performed to elucidate the impact of these adverse conditions on the effective signal-to-noise ratio (SNR) of the high-power reacting flow

velocity data. The mean normalized correlation strength and mean correlation peak ratio (the ratio of the primary to secondary correlation peaks in the crosscorrelation plane) of the computed instantaneous velocity fields measured in flame B were 0.36 ± 0.04 and 2.0 ± 0.63 , respectively, sampled over 3500 measurements. While the instantaneous, peak correlation values were comparable between the reacting and nonreacting cases, the mean correlation SNR is considerably reduced from the nonreacting flow measurements, which consistently yielded mean normalized correlation peaks > 0.6 and peak ratios > 3.0 , respectively. The correlation noise floor was 0.078 ± 0.022 , which was computed from a series of unseeded, nonreacting flow images. It should be noted, by masking the inlet reactant flows (where droplet presence is high), the mean values in the reacting flow case were effectively biased to the burned gas regions. Uncorrelated random background noise, from flame luminosity, decreases the contrast of the small or weakly illuminated particles while the effect of density gradients within the internal flame structure is to blur both the particle image and the correlation peak. As flame power is increased, the defocusing effects become stronger and the effectiveness of the previously described preprocessing algorithm is reduced. While increasing the final interrogation window size (at the loss of vector resolution) did extend the range over which useful measurements were acquired, the adverse effects became so severe that applications at thermal power > 1.0 MW were not attempted.

For validation, an estimation of the volumetric flow rate was computed by integration of the measured velocity field near the burner face. Comparison to the metered total incoming mass flow rate showed agreement consistently within ± 10 % for the nonreacting flow studies. In addition to the intrinsic uncertainties of the measurement technique, integration errors arising from unresolved out-of-plane variation in the swirling flow are expected to be the primary source of this discrepancy. When applied to the reacting flow measurements, the integration yielded little insight due to uncertainty in the flow density and the absence of vectors in the droplet-masked regions of the reactant supply jets.

4.1.2 Measurement resolution of spatial and temporal scales

A sequence of instantaneous velocity field measurements is presented in Fig. 13. As absolute velocities (with the mean flow included), good agreement is seen in the overall structure of the flow between consecutive measurements. Close examination, however, reveals very little temporal correlation between the velocity fluctuations and smaller scale instantaneous structure. Without any foreknowledge of the turbulence characteristics of the flow, a detailed analysis

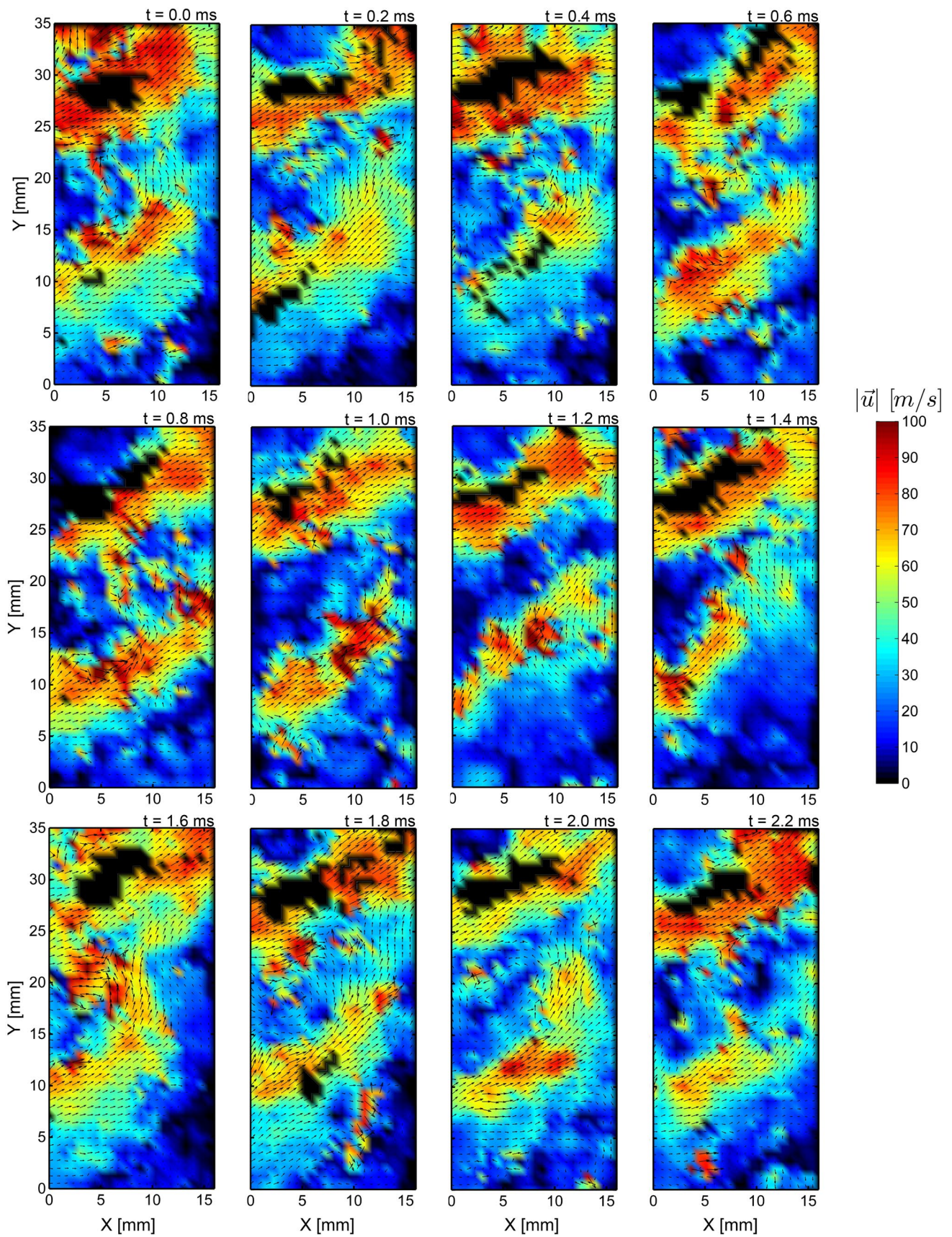


Fig. 13 Sequence of instantaneous velocity field measurements. Black regions have been masked by the droplet filtering operations

was performed to quantify the measurement resolution with respect to the relevant scales.

The velocity autocorrelation function has been extensively used in the past to study the time scales of a turbulent flow. Assuming the convective velocities are much greater than the fluctuations in velocity, Taylor's hypothesis for frozen turbulence can be applied to extract the turbulence length scales from a well-resolved time series of velocity measurements. It is later shown that Taylor's hypothesis is a poor assumption for this flow, but it is sufficient for the purpose of this analysis. Figure 15 presents the two-point correlation computed from the autocorrelation of the velocity fluctuation time series sampled at probe location P5, in the shear layer between the main and pilot jets where droplet filtering will not affect the time series (see Fig. 14). The correlation was computed for both components of velocity, and the length scale r was determined using the respective component of the mean velocity taken at that location. The complete loss of correlation between two consecutive measurements provides clear indication of the lack of temporal resolution with respect to the turbulent time scales of pilot-main shear layer. The analysis was repeated for all of the sample locations indicated in Fig. 14 with consistent results, though droplet filtering limited the utilization of the time series extracted at P1 and P2.

To better characterize the scales of the turbulent flow, a detailed analysis of the nonreacting flow measurements was performed. Direct spatial correlation of fluctuating velocity components measured in a two-dimensional field can provide a measure of the spatial coherence within the flow. These computations must be approached carefully, however, as the implicit assumption is that the turbulence field is statistically homogeneous in nature [3]. The fluctuating velocity field was sampled from a windowed region within the main reactant jet for this analysis: The sampled region of interest was from $x = [0, 17]$ mm and $y = [21, 34]$ mm. The ensemble averaged lateral and longitudinal two-point correlations for operating condition B are given in Figs. 16 and 17, respectively. The similarity of the lateral and longitudinal correlations in the x and y directions gives credence to the notion that the turbulence within this sampled region is well approximated as homogeneous (as well as isotropic) [31, 32].

Consequently, the integral scale can be determined by computation of the integral of the ensemble averaged two-point correlation,

$$\Lambda = \int_0^{\infty} Q_{ij}(r) dr. \quad (1)$$

The integral length scale was found to be $2.8 \text{ mm} \pm 0.2 \text{ mm}$ when computed from the lateral and longitudinal correlations taken in the x and y directions. Approximately half the width of the main annulus height, this result is physically

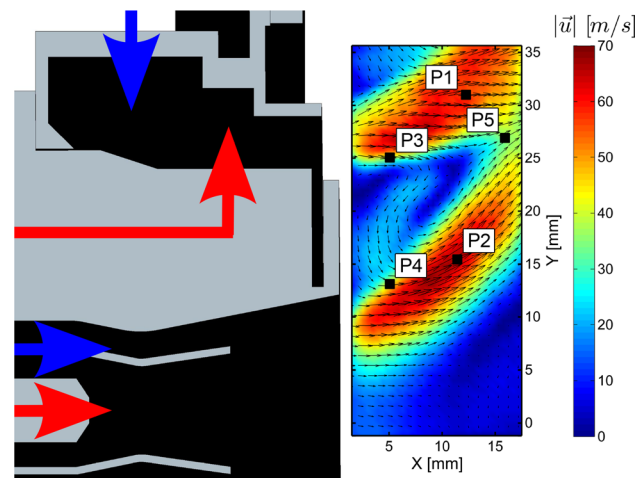


Fig. 14 Mean velocity field with time series probe locations indicated

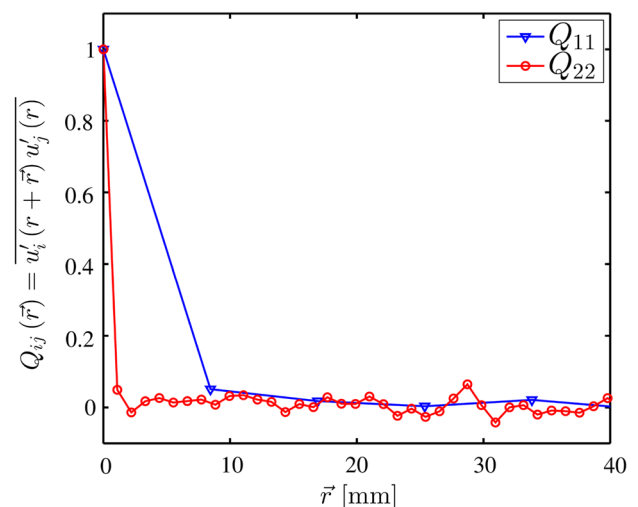


Fig. 15 Autocorrelations of u_1 (blue) u_2 (red) at probe location P5 in a reacting flow field at condition B

feasible and also serves to further confirm the assumptions made in the computation of the discrete spatial correlation.

Returning to the results of the reacting flow autocorrelation: at the sampled location, P5, the mean in-plane velocity magnitude is approximately 40 m/s (see Fig. 14). Disregarding any unresolved out-of-plane effects, over a single $200 \mu\text{s}$ time interval, the fluid element at P5 will convect approximately 8 mm, three times the integral length scale. Evidently, the complete nullification of the autocorrelation is to be expected.

Based on this baseline characterization of the flow under study, it is now critical to evaluate the extent to which these velocity field measurements can be utilized. The PIV measurement technique results in the spatial averaging of the

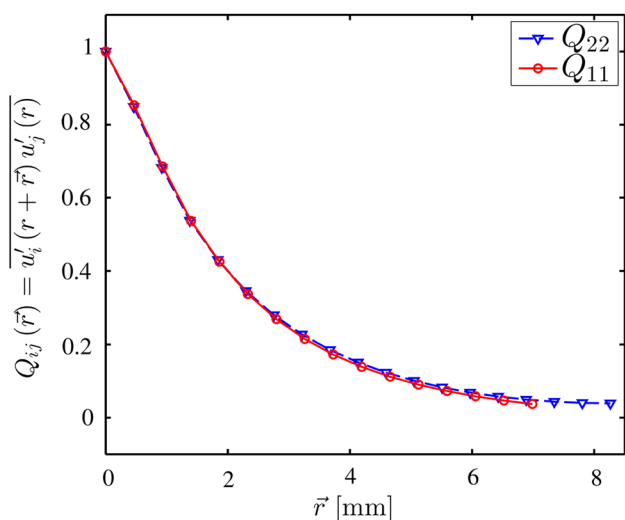


Fig. 16 Lateral two-point velocity correlation in the *x* (blue) and *y* (red) directions at condition B-NR

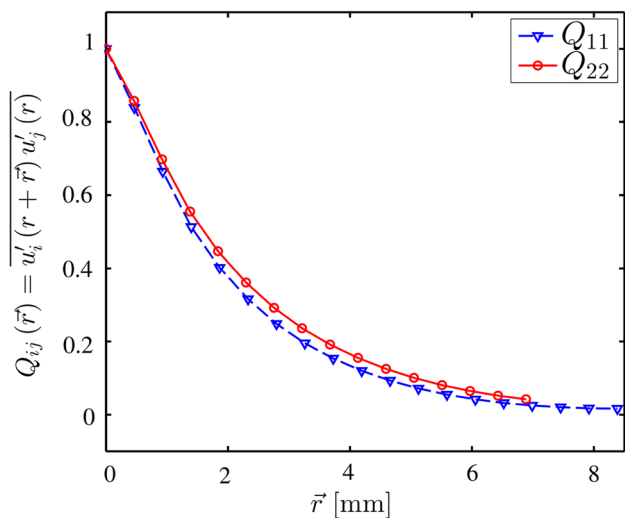


Fig. 17 Longitudinal two-point velocity correlation in the *x* (blue) and *y* (red) directions at condition B-NR

true velocity field, a broadband coherent turbulence spectrum, into discrete measured velocities where the extent of spatial averaging is dependent on the resolution of the interrogation cell. As a result of this loss of length scale resolution, the velocity fluctuations and higher-order statistics of length scales smaller than the interrogation window size are effectively filtered. The measurement errors induced by this filtering process are thus dependent on the range of scales resolved. In the work of Spencer and Hollis [33], it was determined that the turbulent kinetic energy can be measured to within 5 % uncertainty if the grid resolution is ten times smaller than the integral scale. It was also shown that errors as high as 50 % could result from

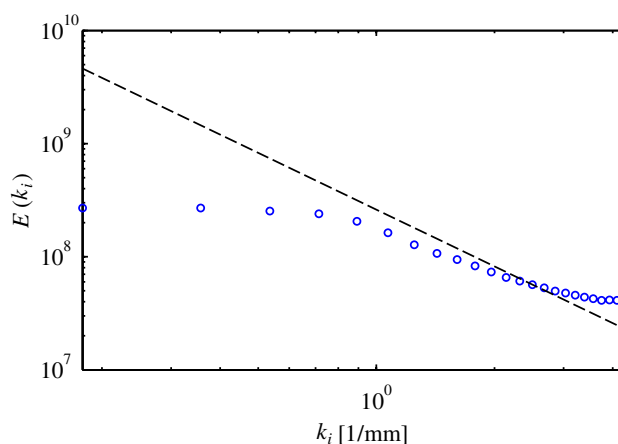


Fig. 18 One-dimensional turbulent kinetic energy spectrum with $\kappa^{-5/3}$ profile indicated at condition B-NR

measurements with a grid resolution that is approximately equal to the integral scale. In the current experiment, the final interrogation window size results in a spatial resolution of 0.940 mm, which extends only three grid points over the span of the integral length scale. With this resolution, there is a high risk of aliasing and large bias uncertainty in any quantitative analysis of flow properties based on spatial gradients (rotation, strain rate), higher-order statistics, and small scale structures. Figure 18 illustrates this fact as the accumulation of noise in the vector generation algorithm and aliasing effects cause a buildup of turbulent kinetic energy at high wavenumbers.

4.2 5 kHz planar laser-induced fluorescence of OH

Planar laser-induced fluorescence (PLIF) is a commonly applied technique used to measure the spatial distribution of a targeted species within a measurement plane. Absorption of temporally, spatially, and spectrally controlled light pump molecules of the targeted species to an excited energy state through an allowed transition. Collisional transfer of energy broadens the structure of the excited energy state to populate neighboring levels. The fluorescence signal is generated by the spontaneous decay from the excited state manifold back to a similar manifold in the ground energy state [34]. Strong intermolecular collisions can cause molecules to decay from the excited energy level back to the ground state without emission of a photon through the process of quenching. In the linear regime (see Eq. 2), the fluorescence signal is linearly proportional to the number density of the targeted species in the ground state (n_1^0), the rate of stimulated absorption (W_{12}), and the ratio of the rate of spontaneous emission from the excited state manifold to the ground state manifold ($A_{v'v''}$) to the total rate population decay from the excited state ($A_{v'v''} + Q_{\text{quench}}$) [35]:

$$S_f \propto n_1^0 W_{12} \left(\frac{A_{v'v''}}{A_{v'v''} + Q_{\text{quench}}} \right). \quad (2)$$

In high pressure flames, there are several effects that can lead to difficulty in performing useful PLIF measurements. In theory, the number densities of the targeted species will be greater in high-pressure flames, leading to increased signal levels. In practice, high number densities of absorbing particles in the flame can also lead to significant absorption and attenuation of the excitation laser sheet as it propagates through the medium [36–39]. Re-absorption of the fluorescence signal as it propagates from the probe volume, through the flame, to the detection system is a well-known effect that can also become more pronounced under high-pressure conditions [37, 40]. Increased occurrences of collisional processes act as damping effects which broaden the frequency width of the resonance susceptibility, reducing the peak strength of the coupling between the transition and the incident laser field. This effect is captured in the W_{12} term of Eq. 2 and causes lower signal strength [41]. It is noted that the reduced coupling strength could be beneficial in experiments where the laser sheet attenuation is strong. By pumping a weaker transition, the rate of stimulated absorption (W_{12}) will be reduced, thereby decreasing the laser power attenuation as it propagates through the medium and decreasing the spatial variation in signal-to-noise ratio (SNR) in the direction of sheet propagation.

Figure 19 provides a comparison of the single-shot OH-PLIF signal quality for three different flame conditions studied in this work. In each image, the laser sheet is propagating in the negative Y direction. The images have been corrected for distortion, cropped, and scaled to engineering units. A white-field normalization has also been performed to correct for pixel-to-pixel variation in the image intensity caused by nonuniformity in the HS-IRO/CMOS detection system.

It has been shown that the noise characteristics of the HS-CMOS/IRO detection systems can be very difficult to quantify accurately [42]. As a detailed characterization was beyond the scope of this work, the detector noise was estimated using a series of homogeneous whitefield images acquired at comparable levels of signal and gain. The single-pixel noise value was established as the standard deviation of the offset-corrected whitefield signal, capturing the broadband, uncorrelated sensor noise. Utilizing this method, the time-averaged peak SNR for the three flame conditions (A-C) shown in Fig. 19 are estimated to be 14.6, 12.7, and 10.3, respectively.

It is of key importance to note that there is no observed change in the signal intensity in the direction of the beam propagation to indicate attenuation of the excitation laser sheet. It stands to reason that, with no observed excitation sheet absorption effects, signal trapping is minimal as well.

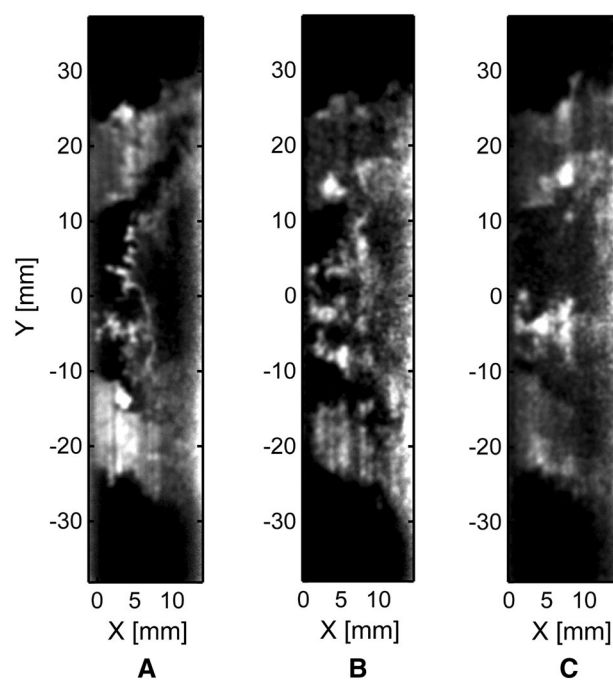


Fig. 19 Raw, single-shot PLIF images from flames A (a), B (b), and C (c)

The extremely high quality of these images, compared to previous high pressure OH-PLIF measurements, is attributed to the advanced nature of the lean burn injector. The design promotes highly effective mixing of fuel and air while utilizing the combination of a central pilot and central recirculation to stabilize the globally lean mixture. It is thought that this highly effective design reduces the number of near-stoichiometric reaction zones near the flame root, serving to reduce the OH mole fractions in the probe volume.

One effect that could contribute to the reduction in signal strength is a decrease in the peak mole fraction of OH at elevated pressure, where increased particle collisions reduce the equilibrium and peak super-equilibrium concentrations through increased three-body collision recombination reaction rates. Collisional broadening of the resonance susceptibility is also thought to be a probable cause of the observed decrease in SNR with increasing combustor pressure. Quantification of these effects on the reduction in the absorption rate (and, consequently, the OH-PLIF signal level) with increasing pressure is the subject of continued work.

The spatial energy profile of the excitation sheet was highly nonuniform, as shown by the vertical streaks in the data images presented in Fig. 19. A series of calibration measurements were performed by imaging the fluorescence signal generated as the sheet propagates through a homogeneous fluorescing medium (acetone vapor). These

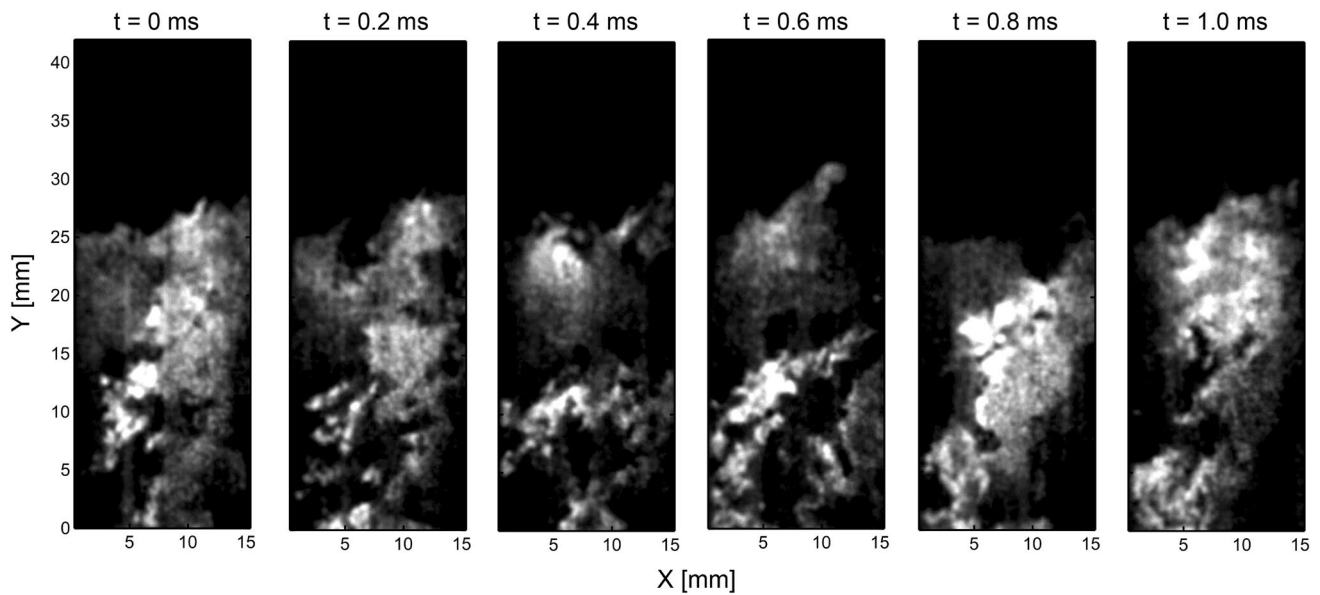


Fig. 20 Sequence of corrected PLIF images at flame B operating condition

calibration measurements indicated multiple peaks in beam energy with shot-to-shot fluctuations in the strength and spatial location. These effects are thought to be the result of local heating within the dye laser doubling crystal as material reabsorbs a fraction of the generated ultraviolet light. During testing, a circulation of oil vapor was seen within the heated cavity of the frequency doubling unit, which was later determined to be emanating from the stepper motor bearings. Deposition and/or burning of these droplets on the surface of the optics could also have contributed to nonuniformities in the beam. Nonetheless, the high degree of signal nonuniformity across the width of the sheet was the result of these shot-to-shot fluctuations, highlighting the need for an in-situ, single-shot sheet correction. In this work, a two-dimensional (2D) spectral filtering technique was utilized to detect and suppress the variation in signal intensity resulting from nonuniformity in the beam energy profile. The details of the procedure are given in Appendix 1. As shown in Fig. 20, the strong structured intensity variations, observed in Fig. 19, were effectively removed.

The key interest in acquiring OH-PLIF measurements in a high-power flame is to extract the spatial coordinates of the reaction front. It has been shown that the spatial gradient of the OH-PLIF signal corresponds well with the interface between burned and unburned gas [43] and, under lean premixed, prevaporized (LPP) conditions, can be used to identify the reaction zones [44]. Consequently, the development of a gradient-based edge-detection method to extract the planar flame surface topography from low SNR OH-PLIF images was of principal interest to this work. Based

on the earlier developments described in Boxx et al. [22], a detailed description of the algorithm is given in Appendix 2.

Applied to the measurements taken in this study, Fig. 21 shows a sample sequence of the computed parametric reaction-front contour functions plotted over the corresponding corrected OH-PLIF image. Good visual agreement is seen between the spatial location of the extracted contour and outer periphery of the corresponding regions of high OH signal intensity. The small breaks in the detected flame surface in regions where the spatial gradient in the OH-PLIF signal remain high are the artifacts of morphological filtering operations, which were required for robust suppression of false-flame edges in the low SNR images. An uncertainty analysis was performed to capture the effects of these operations as well as the user-defined thresholds on the key parameters extracted from the detected flame surface topography. The results are also given in Appendix 2.

5 Results

The quantity and depth of information available with high-repetition-rate measurements can open the path to understanding of new physics, provided the measurement resolution of the targeted scales is sufficient. In this work, it has been shown that the high-power flame under study contains an extremely broad spectrum of spatial and temporal scales that remain highly under-resolved even with the state-of-the-art systems employed. As a consequence, only a baseline analysis of the first-order moments and conditioned statistics of the resolved flow quantities is presented here.

Fig. 21 Reaction-front contour overlaid against corrected OH-PLIF image sequence acquired at the flame B operating condition

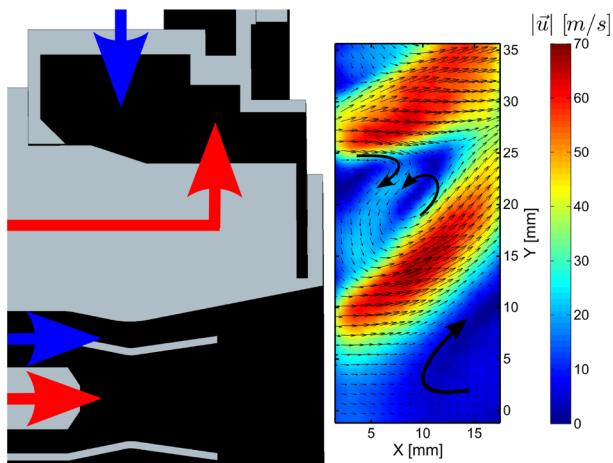
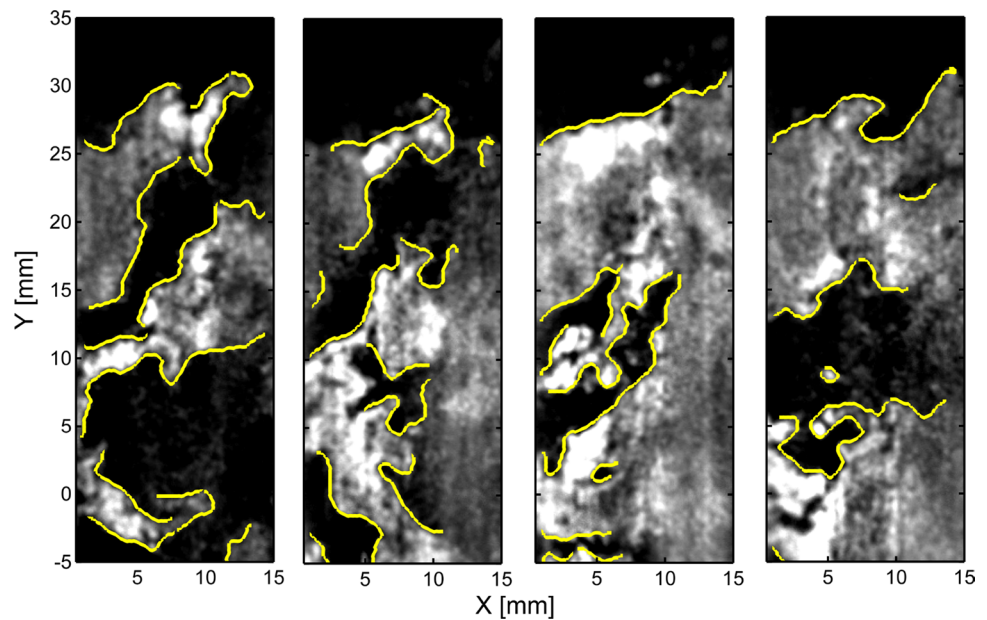


Fig. 22 Mean velocity field acquired at condition B

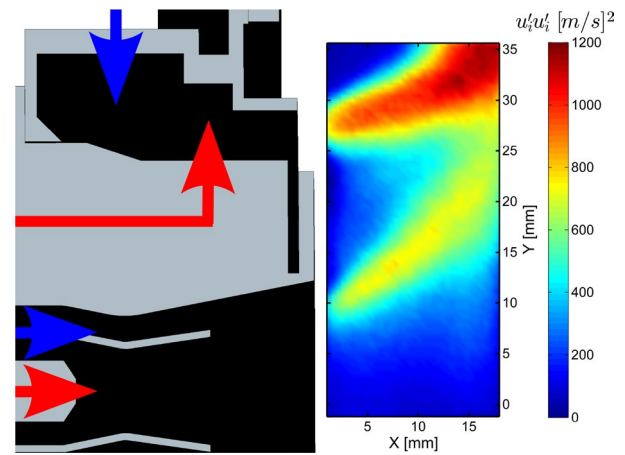


Fig. 23 Mean turbulent kinetic energy field acquired at condition B

5.1 Mean flow structure

The mean velocity field, overlaid against contours of velocity magnitude ($|\mathbf{u}|$), is shown in Fig. 22 with a cross section of the burner schematic shown in Fig. 1 for reference. The mean velocity at each location was computed with an independent sample count at each vector location to avoid errors that would be induced by the droplet filtering operations. High axial velocities (and high-velocity magnitude) indicate reactant influx; as expected, this is seen at the pilot and main nozzle exits. A high degree of swirl causes strong radial (u_r) and azimuthal (not resolved) components of velocity. The two swirling jets converge approximately fifteen millimeters downstream of the burner face, where high-temperature combustion products from the pilot flame

interact with the main reactant supply to stabilize the main flame. The global swirl-induced vortex breakdown of the converged pilot-main flows creates a large central recirculation zone, partially captured in Fig. 22 and indicated by the large arrow near the flow centerline. This low velocity region entrains high-temperature combustion products and transports them back to the pilot flame root, achieving a global stabilization effect on the flame [24]. A secondary pair of counter-rotating toroidal vortices (elliptical in the measurement plane) are also generated downstream of the bluff body. These two features are thought to serve a similar role to the central recirculation zones, providing some degree of preheating to the incoming reactant gases through mixing with high-temperature gases in the shear layers.

Figure 23 illustrates the spatial distribution of the turbulent kinetic energy ($u'_i u'_i$), in the flow. The velocity

fluctuation was computed with a Reynolds decomposition, utilizing the mean velocity field shown in Fig. 22. As expected, the highest turbulence intensities are found within the reactant supply jets. Throughout the length of the two jets, the turbulent kinetic energy of the main reactant jet is approximately 25 % greater than that measured in the pilot jet. This is a result of the fact that the main jet is composed primarily of unburned reactant mixture, whereas the region of the pilot jet often contains burned gas from the pilot injection of the central recirculation zone (see Figs. 20, 21). The increased viscosity of the burned gas in this region will lead to the dampening of the velocity fluctuations in the pilot jet, resulting in decreased turbulence despite having very similar velocity magnitudes and spatial scales to the main jet.

At $x > 12$ mm and $y > 30$ mm, the turbulent kinetic energy reaches a maximum in the main jet. The leading edge of this region corresponds with the axial location of the saddle point generated by the recirculation zones downstream of the aft heat-shield and the leading edge of the shear layer between the pilot and main jets. Evidently, this region is also near the leading edge of main heat release zone, which develops just downstream of the field of view. Intermittent turbulent diffusion and propagation of the main flame leading edge near the downstream limit of the measurement domain leads to rapid fluctuations in gas density and acceleration of the flow in this region, as evidenced by the high turbulent kinetic energy.

Although the spatial resolution of the PIV measurements restricts the utilization of spatial gradient-based quantities in the instantaneous velocity fields, these values are well resolved in the mean velocity field and yield valuable insight to the internal flow structure. It is well-known that the velocity gradient tensor can be decomposed into isotropic, symmetric, and anti-symmetric tensors as follows:

$$u_{ij} = \frac{1}{3} \Delta \delta_{ij} + S_{ij} + \Omega_{ij} . \tag{3}$$

The deformation of a fluid element is described by the strain-rate tensor S_{ij} , defined as

$$S_{ij} = \frac{1}{2} (u_{i,j} + u_{j,i}) - \frac{1}{3} \Delta \delta_{ij} , \tag{4}$$

where the $\frac{1}{3} \Delta \delta_{ij}$ term accounts for dilatation in the velocity field. The anti-symmetric term, Ω_{ij} represents solid body rotation in the flow and is defined by Eq. 5,

$$\Omega_{ij} = \frac{1}{2} (u_{i,j} - u_{j,i}) . \tag{5}$$

The mean out-of-plane vorticity field, $\omega_z = 2\Omega_{21}$, is given in Fig. 24. It clearly shows the presence of a secondary recirculation zone in the form of a counter-rotating vortex

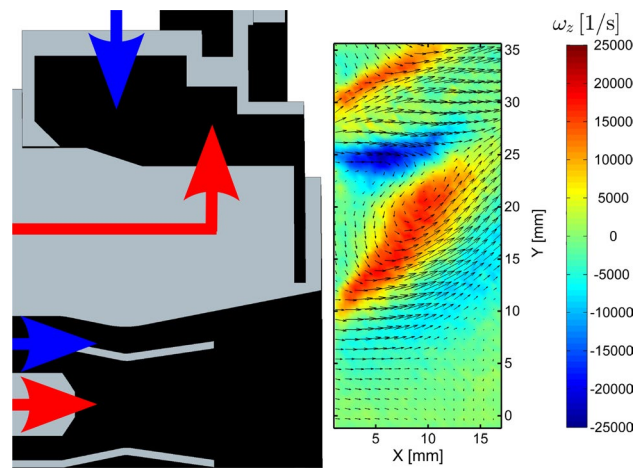


Fig. 24 Mean vorticity field acquired at condition B

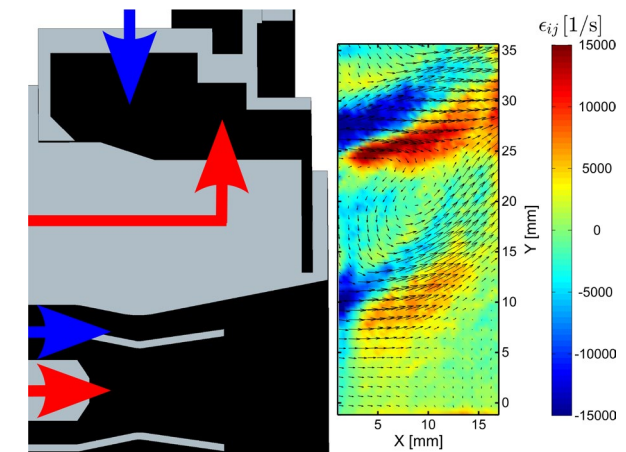


Fig. 25 Mean shear strain-rate field acquired at condition B

pair just downstream of the bluff body, which separates the pilot and main jets. Recirculation of hot combustion radicals from the pilot flame, typically operated fuel rich or near stoichiometric, mixes with the incoming reactants from the main reactant jet. This interaction promotes effective preheating and fuel vaporization along the inner radius of the main reactant jet facilitating ignition and flame stabilization of the main heat release at approximately 15 mm downstream of the burner face where the pilot and main jets combine and at the leading edge of the main heat release zone.

The shear strain rate is given by the off-diagonal terms of S_{ij} . As seen in Fig. 25, there are two regions of high shear strain magnitude in the flow. The first is at the interaction between the pilot reactant jet and the central recirculation zone and the second within the shear layer between the main jet and the secondary recirculation downstream of the bluff-body ring.

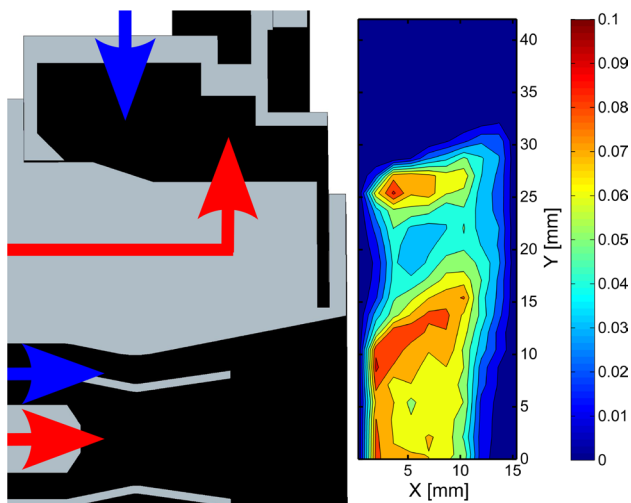


Fig. 26 Mean flame surface density acquired at condition B

5.2 Mean flame structure

The flame surface density is used in computational approaches (under flamelet assumptions) as a means of describing the reaction rate. Defined per unit volume as

$$\Sigma = \frac{\partial A_f}{\partial V}, \quad (6)$$

where A_f is the flame surface area, a planar analog can be computed from experimental data using the reaction-front contour functions extracted from the OH-PLIF images. In this work, the planar flame surface density was computed by dividing the OH-PLIF measurement domain into 1 mm by 1 mm cells (approximately equal to the PIV vector field resolution), then summing the total reaction layer length within each cell. Shown in Fig. 26, the peak values of Σ in the pilot jet are coincident with the regions of high turbulence intensity found in Fig. 23. This is expected as the partially premixed, partially prevaporized reactants enter the chamber and mix with the hot combustion products from the central recirculation zone. A secondary peak in the flame surface density was also detected near the outer radius of the bluff-body ring. Residing in the shear layer between the main jet and the secondary recirculation zone, this peak is coincident with one of the counter-rotating vortices indicated in Fig. 22. Turbulent diffusion from the main reactant supply into this low-velocity region causes intermittent formation of reactant pockets, which ignite after mixing with the hot combustion products recirculating from the pilot flame. The flame then propagates back into the shear layer before being quenched by the high turbulent strain rate at the edge of the main jet. The sequence of OH-PLIF images given in Fig. 20 represents a unique case where this process was well-resolved with the 5-kHz interrogation frequency.

5.3 Conditioned flow statistics

The coupled interactions of turbulence and chemistry govern the structure and stability of the flame. Turbulent eddies can wrinkle the reaction front, providing more flame surface area and resulting in higher flame power. Strong turbulence can inhibit reaction progress by stretching the flame front to extinction, quenching the reaction zone with high levels of turbulent strain. In large eddy simulations, most of the interactions between turbulence and chemistry occur on the sub-grid scale and thus require modeling. LES sub-grid models are formulated using statistical arguments, and therefore, it is expected that only statistical quantities will agree in comparisons between experiments and simulations [3, 45].

Described in Appendix 2, an edge-detection procedure was used to accurately map the flame surface topography based on the gradient of the OH-PLIF signal. A mathematically treatable parametric contour function, $f_i = x_{fi}(\xi_i)\hat{x} + y_{fi}(\xi_i)\hat{y}$, is generated which describes the spatial coordinates of the flame front within the measurement plane. With the known spatial coordinates of the reaction zone, heat release conditioned flow statistics sampled from the simultaneously measured velocity field can be used to provide data for the validation of numerical modeling of flow–flame interactions.

Figure 27 provides an illustration of the velocity field (blue vectors) sampled at the flame surface. To account for the difference in resolution between the two measurement techniques, the sampled field is taken as the interpolated value from the four nearest measurements to the spatial location of reaction front.

As discussed previously, the quantities sampled are subject to the instantaneous measurement resolution requirements, with respect to the relevant scales of the flow. Figure 28 shows the probability density of the velocity magnitude measured at the flame front. The data were compiled from 1,000 instantaneous measurement fields, taken at condition B, providing over 10^5 samples for analysis. The plot shows a broad distribution in the velocity magnitude, with a peak between 30 and 32 m/s and a full width at half maximum of 48 m/s. The peak of the PDF is in agreement with the velocity field magnitude and flame surface density plots (Figs. 22, 26, respectively), where reaction zones are shown to occur in the shear layers between the reactant jets and the recirculation zones. The width of the distribution is simply attributed to the broad range of scales present in the highly turbulent flame burning a multi-component liquid fuel.

An orthonormal vector was computed at every flame-front position to describe the orientation of the flame surface within the plane. Computation of the scalar inner product of the sampled flame-front velocity vector and

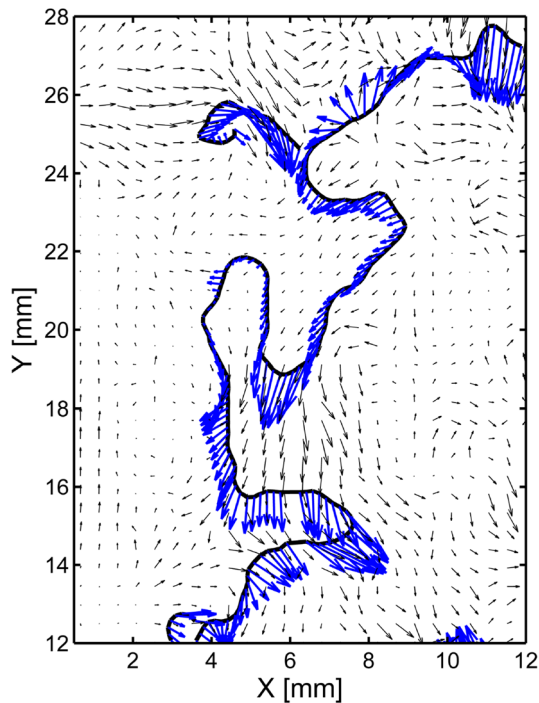


Fig. 27 Conditional sampling of the velocity field at the reaction front by linear interpolation

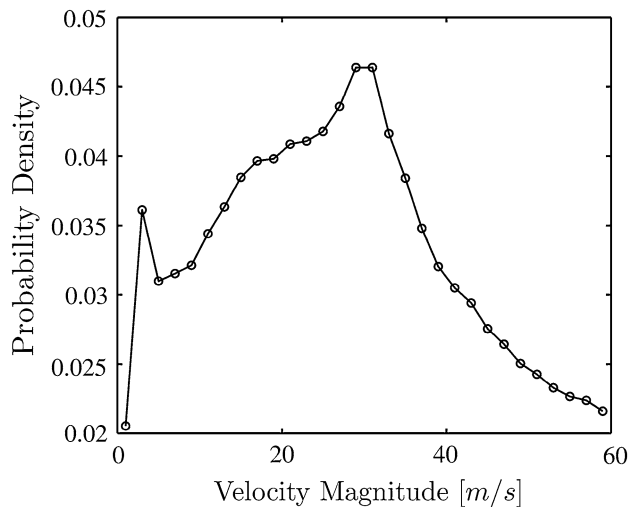


Fig. 28 Probability density of velocity magnitude at the reaction front

the flame-front normal vector yields the velocity magnitude normal to the flame surface. The probability density of the flame surface normal velocity magnitude is given in Fig. 29, which clearly shows an increased probability density of low velocity component normal to the flame surface. Given that the velocity vector magnitude does not show the same peaks in its distribution near zero velocity, this is an

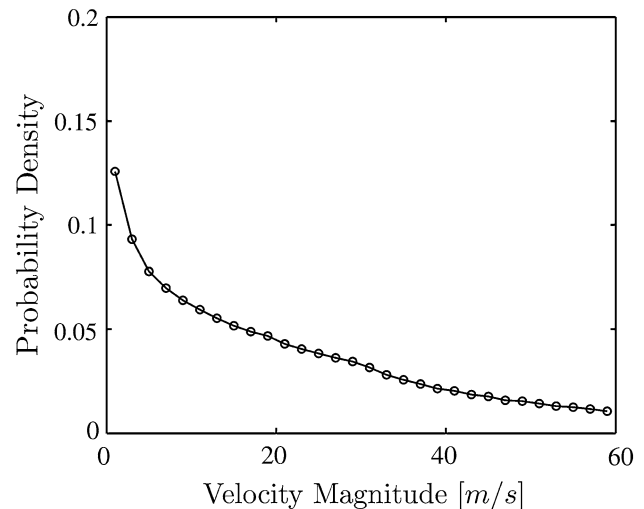


Fig. 29 Probability density of velocity magnitude normal to the reaction front

indication that the flame surface tends to align itself with the local flow velocity vector, i.e., the flame surface normal is perpendicular to the flow direction. This also provides further confirmation that the reaction zone tends to remain in the shear layers between the high-velocity reactant jets and the primary/secondary recirculation zones, which stabilize the flame by entrainment and transport of heat and radicals back to the flame root.

6 Conclusions

Simultaneous measurements of velocity and scalar fields were performed in turbulent nonpremixed flames at gas turbine engine-operating conditions using 5 kHz PIV and OH-PLIF. The quality of the PIV scattering images was shown to be quite good at flame B operating conditions. High thermal power conditions were shown to cause significant defocusing of the particle images as the variations in the optical refractive index of the gas were caused by strong temperature gradients within the inner structure of the flame. High flame luminosity also led to a decreased SNR with increasing flame power. Systematic characterizations of the vector quality were performed to elucidate these effects on the measurement SNR. OH-PLIF measurements did not show indications of strong laser sheet absorption at any condition tested. However, a decrease in the SNR was observed, presumably due to increased collisional broadening, which resulted in a reduced absorption rate. Simultaneous application of 5 kHz PIV and OH-PLIF showed good agreement between single-shot flow-flame interactions, but strong unresolved out-of-plane velocity components restricted the interpretation of the temporal context of single-shot data.

Finally, it was determined that a 5-kHz interrogation frequency offers only low temporal resolution of the turbulent time scales in the high-power flames studied in this work.

Quantitative analysis of high-resolution, high-fidelity measurements is of key importance to the continued progress toward predictive capability in numerical modeling of turbulent flames. At high thermal power density, the vast dynamic range of spatial and temporal scales enforces strict resolution requirements for accurate evaluation of higher-order statistics needed for sub-grid model validation. Falling short of these requirements, the present dataset was used to study the time-averaged flow structure and its effect on flame behavior. Conditional statistical sampling was used to elucidate understanding of the flow–flame interactions in high-power flames.

Acknowledgments This research is funded by GE Aviation and the technical monitors are Dr Michael Benjamin and Dr Sibtos Pal. Carson D. Slabaugh acknowledges the support of the DoD, Air Force Office of Scientific Research, National Defense Science and Engineering Graduate (NDSEG) Fellowship, 32 CFR 168a.

Appendix 1: Spectral filtering

In this work, a two-dimensional (2D) spectral filtering technique was developed to detect and suppress the variation in signal intensity resulting from nonuniformity in the beam energy profile. Similar methods have been shown to successfully mask known spatial frequencies in two-dimensional data, such as in the Structured Laser Illumination Planar Imaging (SLIPI) where an intensity-modulated laser sheet is used to delineate signal photons from noise in

Rayleigh scattering measurements [46]. In this application, calibration images taken in the homogeneous fluorescing medium are used as calibration data to detect the characteristic spatial frequencies of the PLIF laser-excitation sheet. The process is illustrated in Fig. 30 as the operations are demonstrated on a single-shot acetone PLIF calibration image. The raw image (a) is transformed into the frequency domain with a 2D fast Fourier transform (FFT). In the centered 2D Fourier spectrum (b), the coefficients with the low wave numbers are shifted to the middle of the image while the highest frequencies occur at the periphery. The 1D spectral density extracted along $n = 0$ (c) indicates peaks in the power of multiple effective frequencies spatially oriented along the x direction. Suppression of these peaks, followed by computation of the inverse 2D FFT, yields a corrected image (d) with a significant reduction in variation of intensity along the x direction. The computed difference between the corrected data (d) and the raw image (a) is given in Fig. 30e, showing the level of intensity correction performed.

Through development of the 2D spectral filter using the homogeneous-field acetone PLIF images, it was determined that the low-wave-number spatial frequencies measured across the width of the sheet were sufficiently resolved and consistent to be robustly masked on a single-shot basis. Hence, these dominant frequencies were identified using the calibration image set, then applied as a spectral mask on the PLIF data images. The results are shown in Fig. 20 for a sequence of images to show the effective removal of the strong intensity variations previously observed in Fig. 19. It is noted that some high wave number vertical structures have remained in the corrected images (also

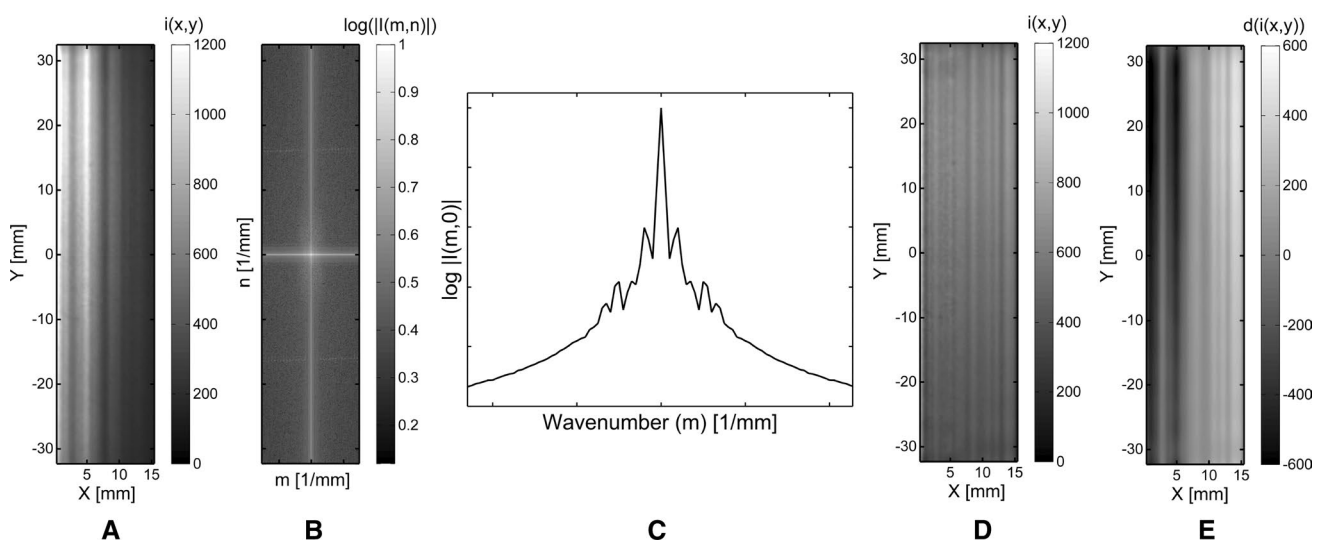


Fig. 30 PLIF sheet intensity correction procedure: raw calibration image (a), centered 2D Fourier spectrum (b), extracted spectrum for horizontal direction (c), corrected calibration image (d), difference between corrected and original (e)

seen in Fig. 30d). It was found that robust suppression of these features was not possible without causing undesirable effects on the corrected images given the spatial resolution of the detection system used in this work.

Appendix 2: Flame surface topography extraction

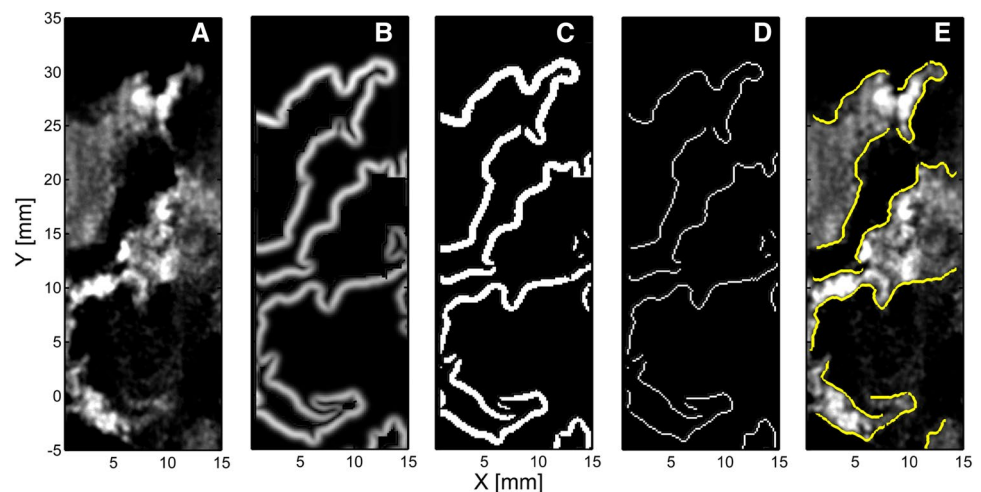
Quantitative detection of the reaction zones using OH-PLIF measurements is a challenging task. While it has been shown that the gradient in the OH-PLIF signal can be utilized as a marker to delineate regions of burned and unburned gas near the reaction zone, these computations are highly sensitive to the image SNR. When utilizing high-repetition-rate, DPSS laser systems, the difficulties stemming from low SNR are exacerbated by the characteristically low laser pulse energies and, consequently, low fluorescence signal levels. High concentrations of OH are also known to remain far downstream in the postflame gases while three-body recombination reactions consume OH on a much slower time scale [18, 44, 47]. In highly turbulent, high-power swirl flames, multiple vortex breakdown recirculation zones are generated (by design) to transport heat and radical back to the flame root for stabilization. In these cases, it can become very challenging to distinguish the OH created at the reaction from the *old* OH that has been recirculated.

In this study, extensive algorithm development was required to accurately and robustly detect the reaction fronts based on the gradient in the OH-PLIF signal. Building on the foundation outlined in Boxx et al. [22], the sheet intensity-corrected OH-PLIF images were first binned with a 2 pixel by 2 pixel square kernel to improve the SNR (Fig. 31a). An edge-preserving nonlinear diffusion filter was then applied to remove uncorrelated detection system noise and low magnitude signal gradients in the burnt gases

[48, 49]. A Gaussian-smoothed spatial gradient was computed from the nonlinear diffusion-filtered image, given in Fig. 31b. It can be seen that the strong gradients correspond well with the boundaries of the regions with high OH signal. However, it can also be seen that there are some regions detected where the signal gradient is quite low, which likely do not represent a flame edge; instead, these edges are likely a pocket of burnt gas or even just signal noise (common near the outer boundaries of the image where convolution filtering operations can cause problems). Hence, the gradient image is binarized with a user-defined threshold on the signal-gradient magnitude, resulting in the logical image given in Fig. 31c. At this stage, a morphological thinning operation was utilized to reduce the broad regions of high OH signal gradient to mathematically treatable contours (Fig. 31d). The utilization of morphological operations in lieu of more *physics-based* methods (e.g., signal-gradient profile curvature) was necessitated by the low PLIF SNR. The result of the procedure is a map of the flame surface topography, defined by the transition for reactants to high OH-PLIF signal. A final filtering operation removes the reaction fronts below a minimum length and multiply-connected *bridge* or *chad* artifacts from the morphological thinning operation. A parametric contour function, $f_i = x_{fi}(\xi_i)\hat{x} + y_{fi}(\xi_i)\hat{y}$, is then generated to describe the spatial coordinates of the flame front within the measurement plane. It should be noted that f_i contains only spatial information about the location of the reaction zone; it is not a direct measure of the reaction rate. As it is seen in Fig. 31, the routine accurately identified the flame edges in the low SNR OH-PLIF images

An uncertainty analysis was performed to capture the effects of varying the user-defined thresholds on the defined flame surface topography. Reporting on condition B, which had a peak SNR of approximately 12.7, variation of the signal-gradient minimum threshold by $\pm 10\%$ resulted in

Fig. 31 Flame surface topography extraction



a $\pm 3.485\%$ maximum response in the total flame contour length and a $\pm 3.92\%$ change in the peak flame surface density. Sweeping the gradient threshold $\pm 25\%$ resulted in a difference as high as 13% in the summed total flame-front length as much as 28% change in the computed RMS. With large datasets, convergence of the mean standard error was $< 2\%$ for statistical quantities computed from f_i , including the mean flame surface density (sampled at multiple distinct points) as well as the summed total flame contour length.

References

1. T. Poinso, D. Veynante, *Theoretical and Numerical Combustion*, 3rd edn. (CERFACS, Toulouse, 2005)
2. N. Peters, *Turbulent Combustion* (Cambridge University Press, Cambridge, 2000)
3. S.B. Pope, *Turbulent Flows* (Cambridge University Press, Cambridge, 2000)
4. K. Bray, Proc. Combust. Inst. **26**(1), 1–26 (1996)
5. R. Bilger, S.B. Pope, K. Bray, J.F. Driscoll, Proc. Combust. Inst. **30**, 21–42 (2005)
6. R. Barlow, Proc. Combust. Inst. **31**, 49–75 (2007)
7. C.F. Kaminski, J. Hult, M. Ald, Appl. Phys. B Lasers Opt. **68**, 757–760 (1999)
8. P. Wu, W.L. Lempert, R.B. Miles, AIAA J. **38**, 672–679 (2000)
9. N. Jiang, R.A. Patton, W.R. Lempert, J.A. Sutton, Proc. Combust. Inst. **33**(1), 767–774 (2011)
10. M.N. Slipchenko, J.D. Miller, S. Roy, J.R. Gord, S.A. Danczyk, T.R. Meyer, Opt. Lett. **37**(8), 1346–1348 (2012)
11. C. Fajardo, J. Smith, V. Sick, Appl. Phys. B **85**(1), 25–30 (2006)
12. I. Boxx, M. Stohr, C. Carter, W. Meier, Appl. Phys. B Laser Opt. Rapid Commun. **95**, 23–29 (2009)
13. C. Abram, B. Fond, A.L. Heyes, F. Beyrau, Appl. Phys. B **111**(2), 155–160 (2013)
14. C.M. Arndt, J.D. Gounder, W. Meier, M. Aigner, Appl. Phys. B **108**(2), 407–417 (2012)
15. B. Bohm, C. Kittler, A. Nauert, A. Driezler, in *Proceedings of the European Combustion Meeting*, (2007)
16. G. Hartung, J. Hult, R. Balachandran, M.R. Mackley, C.F. Kaminski, Appl. Phys. B **96**(4), 843–862 (2009)
17. W. Meier, I. Boxx, M. Stöhr, C.D. Carter, Exp Fluids **49**, 865–882 (2010)
18. A.M. Steinberg, I. Boxx, M. Stöhr, C.D. Carter, W. Meier, Combust. Flame **157**(12), 2250–2266 (2010)
19. M. Stöhr, I. Boxx, C.D. Carter, W. Meier, Combust. Flame **159**(8), 2636–2649 (2012)
20. P. Trunk, I. Boxx, C. Heeger, W. Meier, B. Böhm, A. Driezler, Proc. Combust. Inst. **34**(2), 3565–3572 (2013)
21. C.D. Carter, S. Hammack, T. Lee, Appl. Phys. B Lasers Opt. **116**, 515–519 (2014)
22. I. Boxx, C.D. Slabaugh, P. Kutne, R.P. Lucht, W. Meier, Proc. Combust. Inst. (2014). doi:10.1016/j.proci.2014.06.090
23. C.D. Slabaugh, A.C. Pratt, R.P. Lucht, S.E. Meyer, M. Benjamin, K. Lyle, M. Kelsey, Am. Inst. Phys. Rev. Sci. Instrum. **85**(3) (2014). doi:10.1063/1.4867084
24. A.H. Lefebvre, D.R. Ballal, *Gas Turbine Combustion*. (CRC Press, Taylor & Francis, New York, 1998)
25. M. Raffel, C. Willert, S. Wereley, J. Kompenhans, *Particle Image Velocimetry: A Practical Guide. Experimental Fluid Mechanics* (Springer, London, 2007)
26. R. Adrian, J. Westerweel, *Particle Image Velocimetry. Cambridge Aerospace Series* (Cambridge University Press, Cambridge, 2010)
27. J. Westerweel, *Digital Particle Image Velocimetry: Theory and Application* (Delft University Press, Delft, 1993)
28. F. Picano, F. Battista, G. Troiani, C.M. Casciola, Exp. Fluids **50**(1), 75–88 (2010)
29. N.T. Clemens, M.G. Mungal, Exp. Fluids **185**, 175–185 (1991)
30. M. Samimy, S.K. Lele, Phys. Fluids A Fluid Dyn. **3**(8), 1915–1923 (1991)
31. G.-H. Wang, R. Barlow, N. Clemens, Proc. Combust. Inst. **31**(1), 1525–1532 (2007)
32. B. Ganapathisubramani, N.T. Clemens, D.S. Dolling, J. Fluid Mech. **556**, 271–282 (2006)
33. A. Spencer, D. Hollis, Meas. Sci. Technol. **16**(11), 2323–2335 (2005)
34. R.P. Lucht, D.W. Sweeney, N.M. Laurendeau, Combust. Flame **50**, 189–205 (1983)
35. A.C. Eckbreth, *Laser Diagnostics for Combustion Temperature and Species* (Taylor and Francis, New York, 1996)
36. J. H. Frank, M. F. Miller, M. G. Allen, in *Aerospace Sciences Meeting*, (1999)
37. D. Salgues, G. Mouis, S.-Y. Lee, D. M. Kalitan, S. Pal, R. Santoro, in *Aerospace Sciences Meeting and Exhibit*, (2006).
38. U. Stopper, M. Aigner, W. Meier, R. Sadanandan, M. Stohr, I.S. Kim, J. Eng. Gas Turbines Power **131**(2), 021504 (2009)
39. U. Stopper, W. Meier, R. Sadanandan, M. Stöhr, M. Aigner, G. Bulat, Combust. Flame **160**(10), 2103–2118 (2013)
40. R. Sadanandan, W. Meier, J. Heinze, Appl. Phys. B Lasers Opt. **106**, 717–724 (2012)
41. A.E. Siegman, *Lasers* (University Science Books, Mill Valley, 1986)
42. V. Weber, J. Brubach, R.L. Gordon, A. Driezler, Appl. Phys. B Lasers Opt. **103**, 421–433 (2011)
43. M. Sweeney, S. Hochgreb, Appl. Opt. **48**(19), 3866–3877 (2009)
44. R. Sadanandan, M. Stohr, W. Meier, Appl. Phys. B Opt. Lasers **90**, 609–618 (2008)
45. S.B. Pope, N. J. Phys. **6**, 35–35 (2004)
46. E. Kristensson, A. Ehn, J. Bood, M. Aldn, Proc. Combust. Inst. (2014). doi:10.1016/j.proci.2014.06.056
47. I. Boxx, M. Stohr, C. Carter, W. Meier, Combust. Flame **157**, 1510–1525 (2010)
48. P. Perona, J. Malik, IEEE Trans. Pattern Anal. Mach. Intell. **12**(7), 629–639 (1990)
49. J. Weickert, B. Romeny, M. Viergever, IEEE Trans. Image Process. **7**(3), 398–410 (1998)